

## RESEARCH ARTICLE

10.1002/2016JC012052

## Special Section:

Dense Water Formations in the North Western Mediterranean: From the Physical Forcings to the Biogeochemical Consequences

## Key Points:

- The initiation of the autumnal bloom is linked to the mixing of the shallowing summer DCM
- Heat fluxes and restratification of the mixed layer control the spring bloom dynamics
- Deep winter convection events enhance the spring bloom's magnitude by favoring diatoms development

## Correspondence to:

N. Mayot,  
nicolas.mayot@obs-vlfr.fr;  
F. D'Ortenzio,  
dortenzio@obs-vlfr.fr

## Citation:

Mayot, N., F. D'Ortenzio, V. Taillandier, L. Prieur, O. P. de Fommervault, H. Claustre, A. Bosse, P. Testor, and P. Conan (2017), Physical and Biogeochemical Controls of the Phytoplankton Blooms in North Western Mediterranean Sea: A Multiplatform Approach Over a Complete Annual Cycle (2012–2013 DEWEX Experiment), *J. Geophys. Res. Oceans*, 122, 9999–10,019, doi:10.1002/2016JC012052.

Received 13 JUN 2016

Accepted 25 MAR 2017

Accepted article online 31 MAR 2017

Published online 18 DEC 2017

© 2017. American Geophysical Union.  
All Rights Reserved.

## Physical and Biogeochemical Controls of the Phytoplankton Blooms in North Western Mediterranean Sea: A Multiplatform Approach Over a Complete Annual Cycle (2012–2013 DEWEX Experiment)

Nicolas Mayot<sup>1</sup> , Fabrizio D'Ortenzio<sup>1</sup> , Vincent Taillandier<sup>1</sup> , Louis Prieur<sup>1</sup> , Orens Pasqueron de Fommervault<sup>1</sup> , Hervé Claustre<sup>1</sup> , Anthony Bosse<sup>2</sup> , Pierre Testor<sup>2</sup> , and Pascal Conan<sup>3</sup> 

<sup>1</sup>Laboratoire d'Océanographie de Villefranche, Sorbonne Universités, UPMC Univ Paris 06, INSU-CNRS, Villefranche-sur-mer, France, <sup>2</sup>Laboratoire d'Océanographie et du Climat: Expérimentation et Approches Numériques, Sorbonne Universités, UPMC Univ Paris 06, CNRS-IRD-MNHN, IPSL, Paris, France, <sup>3</sup>Laboratoire d'Océanographie Microbienne, Observatoire Océanologique, Sorbonne Universités, UPMC Univ Paris 06, CNRS, Banyuls-sur-mer, France

**Abstract** The North Western Mediterranean Sea exhibits recurrent and significant autumnal and spring phytoplankton blooms. The existence of these two blooms coincides with typical temperate dynamics. To determine the potential control of physical and biogeochemical factors on these phytoplankton blooms, data from a multiplatform approach (combining ships, Argo and BGC-Argo floats, and bio-optical gliders) were analyzed in association with satellite observations in 2012–2013. The satellite framework allowed a simultaneous analysis over the whole annual cycle of in situ observations of mixed layer depth, photosynthetic available radiation, particle backscattering, nutrients (nitrate and silicate), and chlorophyll-*a* concentrations. During the year 2012–2013, satellite ocean color observations, confirmed by in situ data, have revealed the existence of two areas (or bioregions) with comparable autumnal blooms but contrasting spring blooms. In both bioregions, the ratio of the euphotic zone (defined as the isolume 0.415 mol photons  $m^{-2} d^{-1}$ ,  $Z_{0.415}$ ) and the MLD identified the initiation of the autumnal bloom, as well as the maximal annual increase in [Chl-*a*] in spring. In fact, the autumnal phytoplankton bloom might be initiated by mixing of the summer shallowing deep chlorophyll maximum, while the spring restratification (when  $Z_{0.415}/MLD$  ratio became  $>1$ ) might induce surface phytoplankton production that largely overcomes the losses. Finally, winter deep convection events that took place in one of the bioregions induced higher net accumulation rate of phytoplankton in spring associated with a diatom-dominated phytoplankton community principally. We suggest that very deep winter MLD lead to an increase in surface silicates availability, which favored the development of diatoms.

### 1. Introduction

The seasonality of phytoplankton biomass in the North Western Mediterranean Sea (NWM) follows a typical temperate pattern, with a spring bloom followed by summer oligotrophy and a less intense secondary bloom in autumn [Morel and André, 1991; Bosc *et al.*, 2004; Siokou-Frangou *et al.*, 2010; Estrada and Vaqué, 2014; Lavigne *et al.*, 2015b]. Satellite data of chlorophyll-*a* concentration ([Chl-*a*], in  $mg m^{-3}$ , considered as a proxy for phytoplankton biomass) reveal that the temperate cycle found in the Gulf of Lion is different than in the rest of the Mediterranean basin, which displays a typical subtropical cycle [D'Ortenzio and Ribera d'Alcalà, 2009]. In addition, an autumnal bloom is also observed, and it can be related to the deepening of the Mixed Layer Depth (MLD) after summer [Volpe *et al.*, 2012; D'Ortenzio *et al.*, 2014; Mignot *et al.*, 2014; Shabrang *et al.*, 2015].

This winter deepening of the MLD in the NWM takes place mainly in a “mixed patch,” located in the center of the general cyclonic circulation of the area, where open-ocean convective activities occur due to atmospheric forcings [Millot, 1999]. Moreover, various (sub)mesoscale processes are generally associated within the mixed patch [e.g., Lévy *et al.*, 1998, 1999; Testor and Gascard, 2006; Waldman *et al.*, 2017], also generated by instabilities of the fronts and the alongslope circulation [e.g., Alberola *et al.*, 1995; Font *et al.*, 1995; Millot,

1999; Bosse *et al.*, 2015]. In spring, the water column is restratified by the shallowing of the MLD, followed by a strong thermal stratification in summer that concludes the annual cycle of the MLD in the NWM [D'Ortenzio *et al.*, 2005; Houpert *et al.*, 2014]. However, the winter deepening of the MLD presents strong interannual variability. During some winters, events of open-ocean deep convection occur, leading to the formation of the Western Mediterranean Deep Water [e.g., MEDOC Group, 1970; Marshall and Schott, 1999; Houpert *et al.*, 2016]. In other terms, the integrated effects of atmospheric forcings induce a widespread winter deepening of the MLD in the NWM, but the maximal depths reached are greatly variable, depending on the spatiotemporal variability of the atmospheric conditions and of the preconditioning before winter convection [Houpert *et al.*, 2016; Somot *et al.*, 2016].

The variability of winter convective mixing leads to interannual variability in the intensity, timing, and spatial extent of phytoplankton spring blooms [Barale *et al.*, 2008; Marty and Chiavérini, 2010; Olita *et al.*, 2011; Bernardello *et al.*, 2012; Volpe *et al.*, 2012; Herrmann *et al.*, 2013; Lavigne *et al.*, 2013; Estrada *et al.*, 2014; Severin *et al.*, 2014; Mayot *et al.*, 2016]. However, these previous studies were generally restricted to a specific event [mostly on the basis of cruise data, i.e., Estrada *et al.*, 2014; Severin *et al.*, 2014], or at a fixed site (i.e., at the DYFAMED sampling site, Marty and Chiavérini [2010]), or using satellite data that are limited to surface layer of the ocean [i.e., Barale *et al.*, 2008; Olita *et al.*, 2011; Volpe *et al.*, 2012; Lavigne *et al.*, 2013; Mayot *et al.*, 2016]. Therefore, the lack of in situ observations simultaneously inferring the main physical and biogeochemical variables is certainly a major obstacle to unify a consensual description of the variability of the phytoplankton spring bloom and to elucidate the whole phytoplankton annual cycle (from summer to summer). For the moment, and at a large regional scale, this was only achieved by coupling satellite data with model and scarce in situ data [e.g., Chiswell, 2011].

The recent development of autonomous platforms equipped with biogeochemical sensors provided an excellent source of in situ data, and enabled studying the phytoplankton blooms and its annual cycle in more details. At the global scale, biogeochemical autonomous platforms now comprise the majority of the in situ simultaneous observations of physical and biogeochemical properties that is collected [Biogeochemical-Argo Planning Group, 2016]. However, they are still too scarce to provide a complete reconstruction of the biogeochemical fields at the regional scale. For this reason, they have to be accurately spatially and temporally aggregated, depending on the variability of the processes being investigated.

In this context, satellite data represent a powerful tool to divide the ocean into spatial ecological units (or bioregions), which could be then used to contextualize in situ data [e.g., Devred *et al.*, 2007; Frajka-Williams and Rhines, 2010; Lavigne *et al.*, 2013; Lacour *et al.*, 2015]. In other terms, they provide an excellent opportunity to determine how in situ data collected over different periods of time in an area can be analyzed together.

In the NWM, the phytoplankton production exhibits a significant seasonal variability with a large part of the production taking place during the spring bloom [e.g., Marty and Chiavérini, 2002; Uitz *et al.*, 2012]. Knowing that phytoplankton production is essential for marine ecosystems and biogeochemical cycles, the environmental mechanisms controlling its spatiotemporal variability have to be identified. Therefore, the objective of this study is to evaluate, over an annual cycle, the environmental properties that influence the dynamics of the phytoplankton biomass, in the NWM. We will focus on the autumnal and spring blooms, and elucidate the main physical and biogeochemical control processes leading to the seasonal and spatial variability of the phytoplankton biomass.

For this, the role of several physical and biogeochemical properties in regulating the phytoplankton blooms is assessed using year-round in situ observations from the whole NWM area. The annual analysis presented here was possible thanks to the multiplatform approach implemented in the DEWEX (DEep Water formation EXperiment) experiment, carried out between July 2012 and July 2013 (for more details on DEWEX see Testor *et al.*, 2017). During DEWEX, five ship surveys were carried out at different periods of the year, with the sampling strategy encompassing the whole NWM. During most of the periods and between ship surveys, autonomous platform observations (i.e., profiling floats and gliders) were carried out.

The DEWEX experimental plan provided an exceptional density of in situ physical and biogeochemical observations, which were analyzed in the context of large and consistent satellite bioregions [Mayot *et al.*, 2016] (as suggested by *The Mermex Group* [2011]). Note that bioregions are used here as a tool to generate

time series of environmental properties from dispersed and sparse in situ data. Such a large-scale approach, coupling satellite data with in situ measurements, should highlight the large forcing factors affecting the phytoplankton development, by averaging off the small-scale variabilities that might have an effect at a local scale.

## 2. Materials and Methods

### 2.1. Ship Surveys

Five ship surveys were carried out aboard the R/V *Le Suroît* and the R/V *Tethys II*: July 2012 (doi:10.17600/12020030), September 2012 (doi:10.17600/13450150), February 2013 (doi:10.17600/13020010), April 2013 (doi:10.17600/13020030), and July 2013 (doi:10.17600/13450110). The station plan was identical for the five surveys, although the effective number of stations differed between cruises (depending on weather conditions): 63 in July/August 2012, 34 in September 2012, 54 in February 2013, 66 in April 2013, and 32 in July 2013 (Figure 1).

Surface to bottom profiles of pressure, temperature, conductivity, and chlorophyll fluorescence were collected at each station. Profiles were derived from continuous measurements performed with conductivity-temperature-depth sensors (CTD, SeaBird's 911plus) and a chlorophyll-*a* measuring fluorometer (Chelsea AcquaTrack). Discrete water samples were collected at 12 pressure levels with 12 L Niskin bottles, from which [Chl<sub>a</sub>] (at 61 stations), particulate organic carbon (POC, at 13 stations), nitrate (NO<sub>3</sub>), and silicate (Si(OH)<sub>4</sub> at 121 stations) were measured. Only the measurements from offshore stations (bathymetry greater than 1000 m) and that were performed inside the studied bioregions (see section 2.4) were used in the present study.

### 2.2. Autonomous Platforms: Argo Floats, BGC-Argo Floats and Bio-Optical Gliders

The ship surveys were supplemented by numerous autonomous platforms, which were deployed to provide measurements between cruises. These include 13 Argo floats (between July 2012 and July 2013, 493 profiles collected), 5 BGC-Argo floats (between September 2012 and July 2013, 292 profiles collected), and 10 bio-optical gliders (between September 2012 and July 2013, 2113 profiles collected) (Figure 1).

Argo and BGC-Argo floats are autonomous profiling floats that drift at depth and collect measurements during upward casts from 1000 or 2000 m to the surface. These casts generally take place at noon, every day or every 5–10 days. Bio-optical gliders are steerable, autonomous platforms that perform measurements in the water column along a saw-tooth trajectory between the surface and a maximum depth of 1000 m, each profile being separated by approximately 2–4 km and 2–4 h. For all these platforms, only profiles with measurements obtained from the surface down to 1000 m were kept.

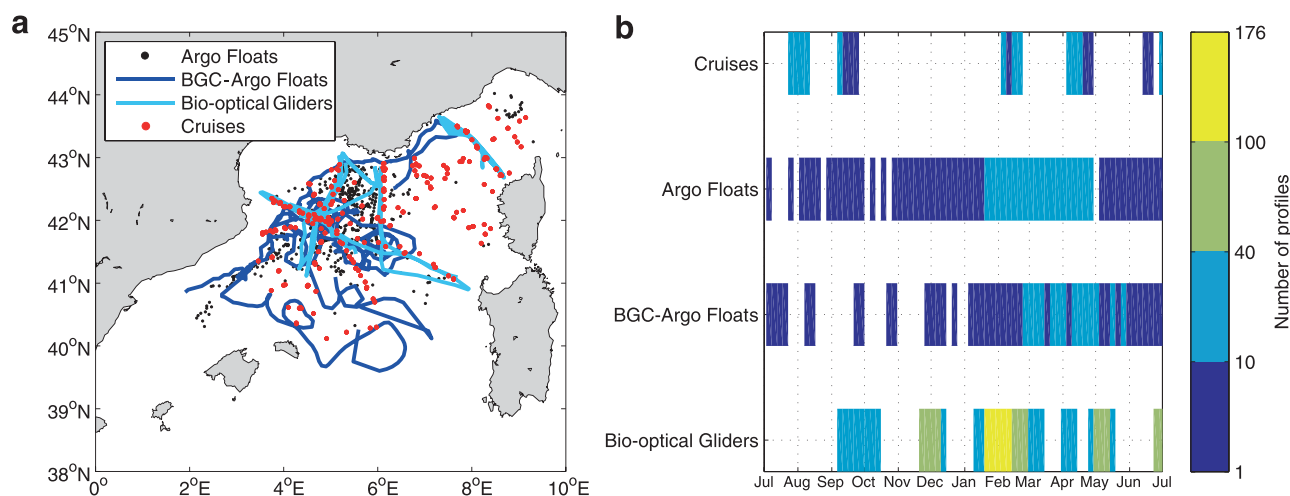


**Figure 1.** (a) Positions of the profiles performed by the different sampling platforms from July 2012 to July 2013. (b) Temporal distribution (5 days bin intervals) of the number of available profiles for each sampling platform. Note the irregular scale of the color bar.

All the autonomous platforms were equipped with CTD sensors (MedArgo Program) [Poulain *et al.*, 2007; <http://doi.org/10.17882/42182>]. Some platforms also carried biogeochemical sensors. Four BGC-Argo floats [Le Traon *et al.*, 2012; Barnard and Mitchell, 2013] and the 10 bio-optical gliders [Niewiadomska *et al.*, 2008; Testor *et al.*, 2010] were equipped with a chlorophyll-*a* measuring fluorometer. Three of the BGC-Argo floats were also equipped with an optical backscattering at 700 nm and a multispectral ocean color radiometer for measuring photosynthetically available radiation (PAR, integrated over 400–700 nm) [Organelli *et al.*, 2016], and one of them carried also a nitrate sensor [Le Traon *et al.*, 2012; Pasqueron de Fommervault *et al.*, 2015a]. A fifth BGC-Argo float only had a nitrate sensor [D'Ortenzio *et al.*, 2012].

### 2.3. Retrieval of Physical and Biogeochemical Properties

Among all the variables measured during the DEWEX experiment, only temperature, salinity, [Chl-*a*], NO<sub>3</sub>, Si(OH)<sub>4</sub>, PAR, and the optical particle backscattering coefficients ( $b_{bp}$ , converts to POC) were specifically analyzed. The choice of these parameters is based on the fact that most of them were measured from both ships and autonomous platforms, which dramatically increased the number of available observations.

#### 2.3.1. Mixed Layer Depth (MLD)

The shipborne temperature and conductivity sensors were corrected for possible drifts, assessed between pre-cruise and post-cruise calibration baths. For the temperature and conductivity sensors of bio-optical gliders, an offset per deployment was estimated by comparing the measurements performed in the deep layers (700–1000 m) with nearby CTD casts collected by the ship or mooring line (the bio-optical glider CTD calibration is fully presented in Bosse *et al.* [2015]). A similar method was used here to calibrate the BGC-Argo float CTD sensors. For Argo floats, only data flagged “good” after a Coriolis data center quality control ([www.coriolis.eu.org](http://www.coriolis.eu.org)) were considered.

The potential density was then derived from pressure, temperature, and conductivity. For each available density profile, the MLD was estimated with a density criterion of 0.01 kg m<sup>-3</sup> (using the 10 m data as reference). Indeed, Houpert *et al.* [2016] argued that a fine criterion is needed to better represent the winter deep mixed layer of the Gulf of Lion due to its weak stratification. When a profile was found to be completely homogeneous according to this criterion, the MLD is associated to the maximal depth of the profile (i.e., 1000 m) even though it might have been deeper.

#### 2.3.2. Chlorophyll-*a*

The [Chl-*a*] was evaluated in the discrete water samples collected with Niskin bottles. For this, between 0.62 and 3.2 L of water samples were filtered onto glass fiber filters (GF/F Whatman 25 mm), that were then stored at –80°C until further analysis at the Oceanography Laboratory of Villefranche-sur-mer. The phytoplankton pigments, including the chlorophyll-*a*, were extracted from the filters in 100% methanol, disrupted by sonication and clarified by filtration (GF/F Whatman 0.7 μm) and finally separated and quantified by high-performance liquid chromatography (HPLC) for further details, see Ras *et al.* [2008].

The [Chl-*a*] was also estimated with chlorophyll-*a* measuring fluorometers mounted on a CTD-rosette, BGC-Argo floats, and bio-optical gliders. For this, the factory calibrations were first applied to all fluorometers so as to convert the fluorescence signal into a nominal [Chl-*a*].

Second, a three-step postprocessing procedure was applied to all profiles. The first step of the postprocessing consisted in the estimation of a deep offset, corresponding to the median value of fluorescence over the 950–1000 m range. Except for deep mixing conditions, the deep chlorophyll-*a* fluorescence was expected to be null, hence the offset could be removed from the whole profile. The second step consisted in removing spikes by using a median filter. The third and last step corrected the fluorescence profile for nonphotochemical quenching, following the procedure of Xing *et al.* [2012]. Exclusively for bio-optical gliders, only night profiles (between 22 P.M. and 2 A.M.) were used in order to avoid nonphotochemical quenching. These night profiles were also averaged to remove small-scale variabilities.

Finally, each individual platform fluorometer was calibrated with all available simultaneous bottle measurements of [Chl-*a*] (i.e., HPLC estimations) using a least square linear regression. For shipborne fluorometers, the fluorescence measurements at the time of the bottle samplings were used for the linear regression. For autonomous platforms, only fluorescence profiles performed on the same day as the water sampling cast, and within a spatial radius lesser than 35 km, were retained for the regression. On average, the spatio-temporal lag between the fluorescence profiles and the sampling casts were 13 h and 12.5 km. It is noteworthy that the fluorescence values around the depth of available bottle samples (±5 m) were averaged

**Table 1.** Result of the Linear Regressions for the Calibration of the Fluorimeters<sup>a</sup>

Name	<i>n</i>	<i>r</i> <sup>2</sup>	Scaling Factor (Slope)
<i>Ship Cruises</i>			
MOOSE-GE 2012	283	0.95	3.50
DOWEX 2012	127	0.71	1.51
DEWEX 2013—Leg 1	225	0.98	2.17
DEWEX 2013—Leg 2	264	0.98	2.03
MOOSE-GE 2013	80	0.93	3.18
<i>BGC-Argo floats</i>			
SBEE	16	0.81	0.44
NAOS 001	11	0.97	0.65
NAOS 017	13	0.86	0.88
NAOS 035	18	0.96	0.59

<sup>a</sup>All the scaling factor values were significantly different from 0 (*t* test, *p* value < 0.001). See section 2.3.2 for more details.

and fluorescence were unavailable to align the platform fluorometer with the bottle measurements, a calibration method using satellite ocean color data was used instead [Lavigne *et al.*, 2012]. This was only the case for bio-optical glider fluorimeters. The calibration obtained from this method was tested against the one using the bottle measurements. To do so, the calibration of Lavigne *et al.* [2012] was applied to the whole dataset of fluorescence profiles and compared to the bottle measurements associated with these fluorescence profiles. Both calibrations gave satisfying and similar results (MADP of 23% with HPLC and MADP of 38% with satellite), thus supporting the use of the method of Lavigne *et al.* [2012] when direct comparison with in situ data was not possible.

### 2.3.3. Nitrate and Silicate

To evaluate NO<sub>3</sub> (±0.02 μM) and Si(OH)<sub>4</sub> (±0.05 μM) concentrations (as detailed in Severin *et al.* [2014]), 20 mL of seawater were immediately filtered on board (using 0.45 μm cellulose acetate filters) and stored in 20 mL polyethylene vials at −20°C until analysis. In the laboratory, samples were rapidly thaw and analyzed by colorimetry on a Seal-Bran-Luebbe autoanalyzer AA3 HR, according to Aminot and Kérouel [2007].

Two BGC-Argo floats were equipped with a nitrate sensor (SUNA), which measured the in situ [NO<sub>3</sub>] by measuring the UV absorption spectrum over the 217–240 nm range [Johnson and Coletti, 2002]. Several possible algorithms exist for deconvoluting [NO<sub>3</sub>] from the observed UV absorption spectrum [e.g., Johnson and Coletti, 2002; Sakamoto *et al.*, 2009; Zielinski *et al.*, 2011]. For the first BGC-Argo float (PROVOR-SUNA), only the processed data were transmitted (i.e., [NO<sub>3</sub>] computed by the manufacturer algorithm), and a specific calibration was developed that accounted for temperature and salinity corrections (fully explained in D'Ortenzio *et al.* [2014]). For the second BGC-Argo float, [NO<sub>3</sub>] as well as raw data (i.e., absorbance spectrum) were transmitted, allowing for data reprocessing with the modified Sakamoto algorithm [Pasqueron de Fommervault *et al.*, 2015a]. The two sensors were then calibrated by using in situ data, and resulted in a detection limit of ~1 μM [see D'Ortenzio *et al.*, 2014; Pasqueron de Fommervault *et al.*, 2015a, for details]. The [NO<sub>3</sub>] in the MLD was averaged ([NO<sub>3</sub>]<sub>MLD</sub>) by using the corresponding MLD values.

### 2.3.4. Particulate Organic Carbon

For 13 stations performed during DEWEX cruises, POC concentration ([POC]) was estimated from the discrete bottle samples. For this, POC was collected on precombusted (24 h, 450°C) glass fiber filters (Whatman GF/F, 25 mm). Filters were dried in an oven at 50°C and stored in ashed glass vial and in a dessicator until analysis in laboratory on a CHN autoanalyser.

Several studies demonstrated that the [POC] can also be estimated from *b*<sub>bp</sub> [e.g., Loisel *et al.*, 2001; Cetinić *et al.*, 2012]. Therefore, from optical backscattering mounted on BGC-Argo floats, the *b*<sub>bp</sub> was computed following the protocol of Schmechtig *et al.* [2015] to estimate POC. Spikes from the resulting *b*<sub>bp</sub> profiles were first removed with a five points median filter followed by a seven points moving average [Briggs *et al.*, 2011]. Following the same procedure as the chlorophyll-*a* measured by the BGC-Argo fluorimeters (see section 1.3.2), *b*<sub>bp</sub> was converted into POC with factors of calibration obtained by comparing *b*<sub>bp</sub> data with simultaneous bottle measurements of [POC], using a least square linear regression. For this, data from all BGC-Argo floats were used together to obtain a unique linear regression: POC = 54,463 × *b*<sub>bp</sub> − 1.19 (*n* = 33 and *r*<sup>2</sup> = 0.82, *p* value < 0.001).

and kept for the linear regression only when the densities measured from both platforms at the given depth were similar (a density difference lesser than 0.03 kg m<sup>−3</sup>, or 0.01 kg m<sup>−3</sup> for winter mixing conditions). The linear regression provided two coefficients: a scale factor (the slope) and a dark value (the intercept). For each linear regression, the dark value was systematically null (i.e., not statistically different from zero, *t* test, *p* value < 0.001), as an offset had already been applied to the fluorescence profiles during the postprocessing steps. Thus, only the scale factor needed to be applied in order to calibrate the fluorometer (Table 1).

When simultaneous measurements of [Chl-*a*]



### 2.3.5. The Euphotic Zone

The euphotic zone was defined as the isolume depth 0.415 mol photons  $m^{-2} d^{-1}$  ( $Z_{0.415}$ ), because phytoplankton photosynthesis is assumed to be impossible below 0.415 mol photons  $m^{-2} d^{-1}$  [Letelier *et al.*, 2004; Boss and Behrenfeld, 2010; Brody and Lozier, 2014; Cetinić *et al.*, 2015]. This definition is used instead of the depth where the downward PAR irradiance equal 1% of the surface value ( $Z_{1\%}$ ), which only depends on the transparency of the water column.

For this, the daily average PAR irradiance at the surface ( $PAR_0$ , measured from MODIS AQUA satellite at 8 days and 9 km of resolution) is used with a diffuse attenuation coefficient for the downward PAR irradiance ( $K_{PAR}$ ) derived from MODIS AQUA satellite [Chl-a] values ( $[Chl-a]_{sat}$ , at 8 days and 9 km of resolution, see the equation (10) in Morel *et al.* [2007]):

$$Z_{0.415} = \log \left( \frac{0.415}{\alpha \times PAR_0} \right) \left( \frac{1}{K_{PAR}} \right) \quad (1)$$

where  $\alpha$  is the factor correcting the  $PAR_0$  values for transmission through the air-sea interface [Mobley and Boss, 2012]. An in situ evaluation of this  $Z_{0.415}$  estimate was also performed by combining  $PAR_0$  with the PAR profiles recorded by BGC-Argo floats ( $PAR_{float}$ ) and following the same approach as Letelier *et al.* [2004]:

$$PAR(z) = \alpha \times PAR_0 \times \left( \frac{PAR_{float}(z)}{PAR_{float}(0)} \right) \quad (2)$$

where  $PAR(z)$  is the PAR value for a specific depth and  $PAR_{float}$  the instantaneous PAR measured by a BGC-Argo float. For this,  $PAR_0$  data at 1 day and 9 km of resolutions from MODIS AQUA satellite are used.

The interplay between  $Z_{0.415}$  and the MLD was investigated using their ratio ( $Z_{0.415}/MLD$ ). In addition, the "penetration depth" ( $Z_{pd}$ ), i.e., the depth encompassing 90% of the satellite-measured signal [Gordon and McCluney, 1975], is derived as  $Z_{pd} = Z_{1\%} \times 4.6$  [Morel and Berthon, 1989].

### 2.4. A Satellite-Based Bioregionalization of the NWM

In situ observations of physical and biogeochemical properties are sparse and dispersed over a large region (Figure 1). They were thus grouped selectively over biogeochemical-coherent areas in order to generate unique time series for each of them. For this, a satellite-based bioregionalization was used.

Here the recent bioregionalization of the Mediterranean basin based on  $[Chl-a]_{sat}$  was chosen [Mayot *et al.*, 2016]. More precisely, this bioregionalization considered a climatological analysis [D'Ortenzio and Ribera d'Alcalà, 2009] to provide bioregions at the annual time scale. The positions of the bioregions present in the NWM according to Mayot *et al.* [2016], between July 2012 and July 2013, were extracted (Figure 2a), in addition to their associated mean annual time series of  $[Chl-a]_{sat}$  (Figure 2b, data at 8 days and 9 km of resolutions from MODIS AQUA).

This bioregionalization of Mayot *et al.* [2016] (determined on the basis of the shape of the annual cycle of surface [Chl-a]) is used under the hypothesis that similar patterns of surface [Chl-a] reflect comparable variations of physical and biogeochemical properties of the water column. Therefore, all available in situ data of physical and biogeochemical properties (i.e., MLD, [Chl-a],  $[NO_3]$ ,  $[Si(OH)_4]$ , [POC], and PAR) were spatially assembled into bioregions according to their location. We prefer grouping in situ observations on the basis of these bioregions rather than using spatial criteria or using intensively statistical interpolations and analysis methods applied to our data sets.

The availability of density, fluorescence,  $[NO_3]$ , [POC], and PAR profiles throughout the year used to reconstruct these time series of physical and biogeochemical properties is summarized in Figure 3. The period of maximum availability of in situ profiles throughout the year extended from January to June 2013 (Figure 3). Before January 2013, the availability of observations was restricted to the ship survey periods (in August and September 2012) and to the bio-optical glider transects (in December 2012). For the nitrate and POC profiles, data were essentially available after February 2013, through the profiles collected during the two DEWEX cruises (in February and April) and by some BGC-Argo floats that operated in between. The nine profiles from one BGC-Argo float that were performed in a cyclonic eddy in late April were removed: indeed, as the platform undertook measurements when there was a low availability of biogeochemical observations (Figure 3a), a structure completely different from the surrounding environment may have led to a

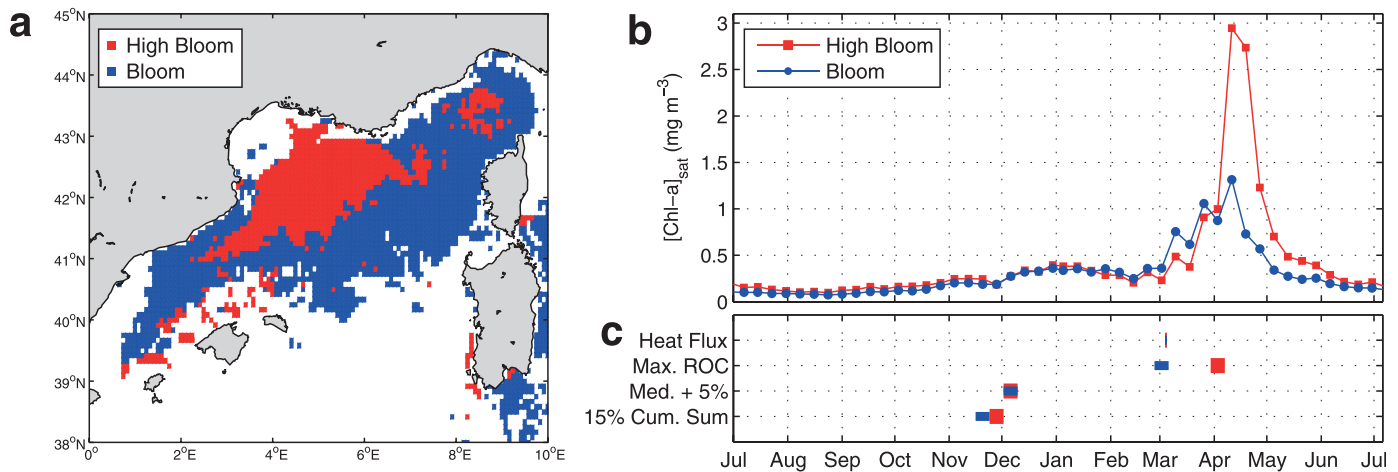


**Figure 2.** (a) Spatial distribution of the two bioregions determined by satellite in the NWM from July 2012 to July 2013. The “Bloom” bioregion is in blue, and the “High Bloom” bioregion is in red. (b) The respective mean time series of  $[Chl-a]_{sat}$  of the two bioregions, (c) with the dates of the phytoplankton blooms derived from different phenological metrics.

misinterpretation. Data were daily averaged and a 5 days median filter was finally applied on the reconstructed time series.

### 2.5. Dates of the Phytoplankton Bloom Initiation

The initiation date of the phytoplankton blooms was determined through three different phenological metrics. Different metrics were used because the inherent variability between them could highlight different periods of the year [Brody et al., 2013; Ferreira et al., 2014].

The first metric was based on the air-sea heat flux (“Heat Flux” criterion) [Ferrari et al., 2015]. According to this criterion, the phytoplankton bloom is initiated with the warming of the ocean (a positive air-sea heat flux). To determine this date, daily air-sea flux data at  $0.125^\circ \times 0.125^\circ$  resolution from ECMWF ERA-interim reanalysis were used [Dee et al., 2011; Donlon et al., 2012]. A time series for each bioregion was then generated by averaging data with a 7 days median filter. After the date of the winter minimum negative heat flux, the date of the onset of the phytoplankton bloom corresponded to the first day with positive air-sea heat fluxes. To discuss the potential influence of the wind, time series of daily wind speed for each

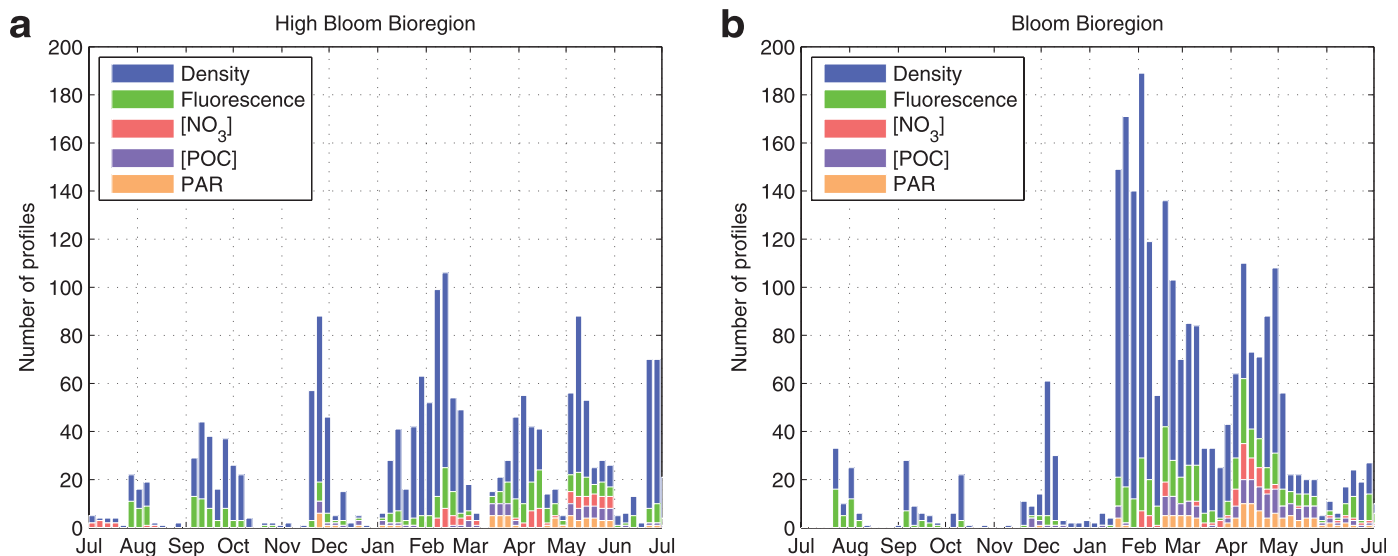


**Figure 3.** Temporal distribution (five days bin intervals) of the number of available density, fluorescence,  $[NO_3]$ ,  $[POC]$ , and PAR profiles, from July 2012 to July 2013, (a) for the “Bloom” and (b) “High Bloom” bioregions.

bioregion was also generated from data available from ECMWF ERA-interim reanalysis, at the same spatial resolution.

The second phenological metric determined the start date as the day when the  $[\text{Chl-a}]_{\text{sat}}$  time series exceeds a certain threshold. Two different thresholds were used here: (1) the semiannual (i.e., from July 2012 to the date of the  $[\text{Chl-a}]_{\text{sat}}$  maximum) median value plus 5% (“median + 5%” criterion, Siegel *et al.* [2002], Brody *et al.* [2013], Hopkins *et al.* [2015]); (2) the 15% of the cumulative sum of the annual  $[\text{Chl-a}]_{\text{sat}}$  (“15% cum. sum.” criterion, Brody *et al.* [2013]).

The third and last phenological metric established the bloom start date as the day displaying the maximal accumulation of phytoplankton biomass (using the  $[\text{Chl-a}]_{\text{sat}}$  as a proxy of the phytoplankton biomass) in the period preceding the date of the  $[\text{Chl-a}]_{\text{sat}}$  maximum. Therefore, the net phytoplankton biomass accumulation rates ( $r$ , also referred to as the rate of phytoplankton biomass changes, e.g., Behrenfeld and Boss [2014]) is used and calculated using the mean  $[\text{Chl-a}]_{\text{sat}}$  time series (as in Lacour *et al.* [2015]):

$$r = \log \left( \frac{[\text{Chl-a}]_{\text{sat}}(t + \Delta t)}{[\text{Chl-a}]_{\text{sat}}(t)} \right) \times \frac{1}{\Delta t} \quad (3)$$

where  $\Delta t$  corresponds to the time interval (here 8 days).

### 3. Results

#### 3.1. Two Distinct Bioregions in the NWM

For the 2012–2013 period, two main bioregions are identified in the NWM, the “High Bloom” bioregion, located in the center of the NWM, and the “Bloom” bioregion, located at its periphery (Figure 2a). These bioregions are characterized by similar patterns in  $[\text{Chl-a}]_{\text{sat}}$  temporal evolution (Figure 2b). Low mean values of  $[\text{Chl-a}]_{\text{sat}}$  are observed during the summer ( $<0.25 \text{ mg m}^{-3}$ ) followed by a slight increase in autumn (in November/December,  $0.3\text{--}0.4 \text{ mg m}^{-3}$ ). Low winter values ( $<0.3 \text{ mg m}^{-3}$ ) are then observed, before a subsequent increase from March to mid-April. The main difference between the two time series can be observed during this last period, with the spring maximal value in  $[\text{Chl-a}]_{\text{sat}}$  clearly lower in the “Bloom” ( $1.3 \text{ mg m}^{-3}$ ) than in the “High Bloom” bioregion ( $2.9 \text{ mg m}^{-3}$ ). After the spring maximum, both bioregions are characterized by a progressive return to a summer oligotrophy (in May, Figure 2b).

For both bioregions, the phenological metrics based on threshold criteria (i.e., “median + 5%” and “15% cum. sum.”) show that the phytoplankton bloom starts in autumn (November/December, Figure 2c). The “Heat Flux” and the “max. ROC” criteria point out a phytoplankton bloom in spring (Figure 2c). However, the “max ROC” criteria indicated a spring bloom one month earlier in the “Bloom” bioregion (2 March  $\pm$  4 days) than in the “High Bloom” bioregion (3 April  $\pm$  4 days).

#### 3.2. Time Series of Physical and Biogeochemical Properties in the Two Bioregions

##### 3.2.1. Heat Flux and Wind Speed

The mean time series of the net heat flux and of the surface wind speed, calculated for the two bioregions, are comparable (Figures 4a and 4b). In summer, positive net heat flux ( $\sim 100 \text{ W m}^{-2}$ ) is associated with relatively low wind speed values ( $<8 \text{ m s}^{-1}$ ), while recurrent strong negative net heat flux ( $<-200 \text{ W m}^{-2}$ ) and wind burst events ( $>8 \text{ m s}^{-1}$ ) are observed in winter. During the transitional periods of spring and autumn, net heat flux values are marked by multiple positive to negative changes around zero, and wind speed is around  $8 \text{ m s}^{-1}$ .

Beyond these similar seasonal trends between the two bioregions, the average intensity in winter of surface heat losses and wind speed are higher in the “High Bloom” bioregion ( $-176 \text{ W m}^{-2}$  and  $8 \text{ m s}^{-1}$ , with daily maximum at  $-376 \text{ W m}^{-2}$  and  $11.9 \text{ m s}^{-1}$ ) than in the “Bloom” bioregion ( $-142 \text{ W m}^{-2}$  and  $7.2 \text{ m s}^{-1}$ , with daily maximum at  $-325 \text{ W m}^{-2}$  and  $10.1 \text{ m s}^{-1}$ ). Interestingly, the winter-spring transition is marked by a first event of positive net heat flux the 5 March, followed by a short event of strong surface heat losses, mainly in the “High Bloom” bioregion ( $-149.8 \text{ W m}^{-2}$ ), before the net heat flux becomes totally positive after the 20 March.

##### 3.2.2. The MLD, the $Z_{0.415}$ and the $Z_{0.415}/\text{MLD}$ Ratio

The seasonal evolution of the MLD in both bioregions is similar (Figure 4c), with a minimum in summer, a progressive deepening in autumn and a maximum reached in late winter followed by a rapid shallowing in



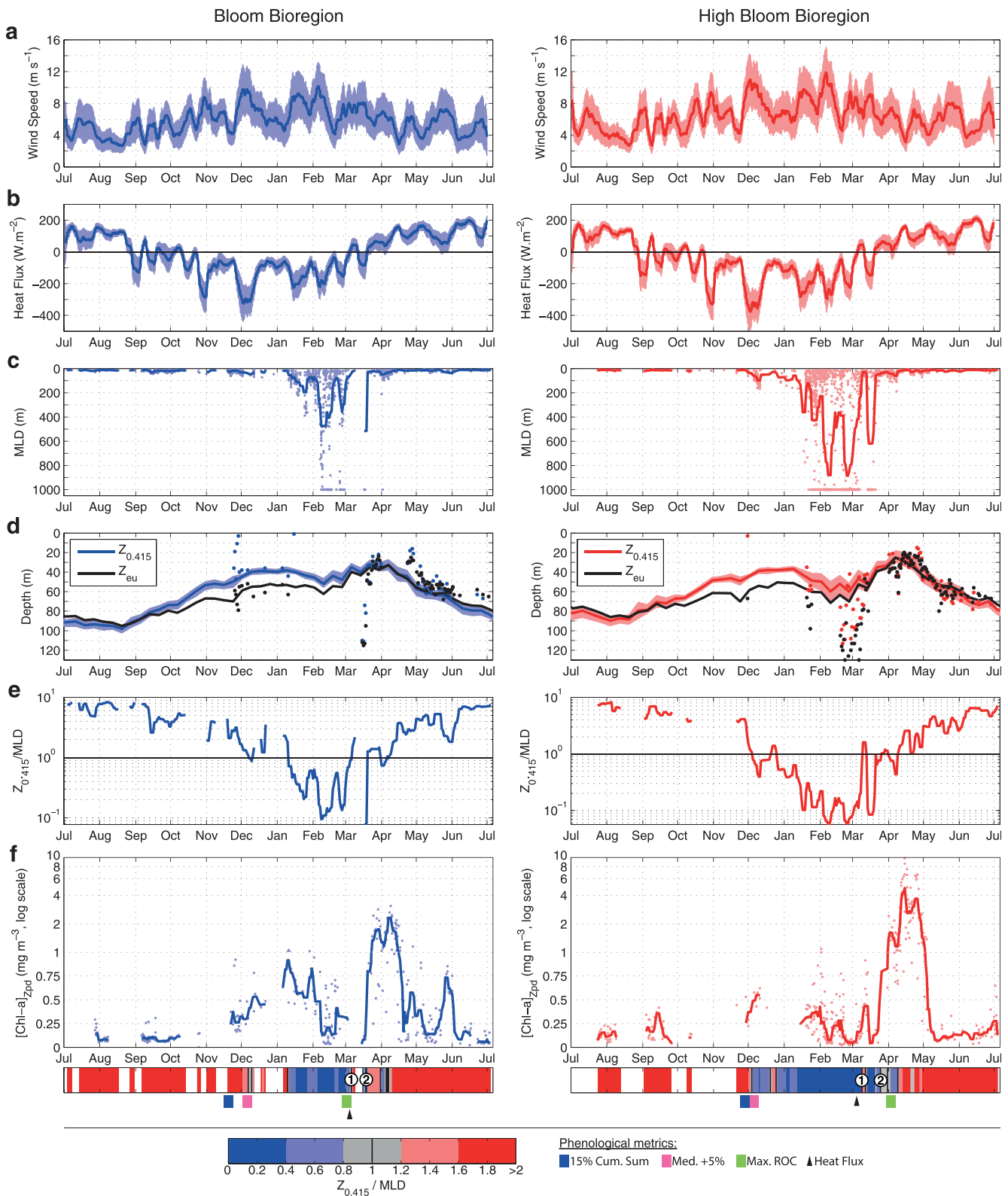


**Figure 4.** Annual time series of physical and biogeochemical properties associated with the two bioregions the “Bloom” (in blue) and “High Bloom” bioregions (in red). Time series of (a) wind speed, (b) heat flux, (c) MLD, (d)  $Z_{0.415}$  and  $Z_{1\%}$ , (e)  $Z_{0.415}/MLD$ , and (f)  $[Chl-a]_{Z_{pd}}$ . The lines represent the mean values median filtered (i.e., 5 days), the dots the single in situ values and the shaded areas the standard deviations. The time series of the  $Z_{0.415}/MLD$  ratio is calculated with the mean  $Z_{0.415}$  and MLD values (i.e., lines in Figures 4c and 4d), and the black line represents when  $Z_{0.415}/MLD = 1$ . The color bars below each plot describe the state of the  $Z_{0.415}/MLD$  ratio, with the phenological metrics from the Figure 2c reported and two spring transition events highlighted (i.e., numbers 1 and 2). Note the logarithmic scale of the y axis for the (e)  $Z_{0.415}/MLD$  ratio, and (f) the  $[Chl-a]_{Z_{pd}}$ .

spring. The main differences between the MLDs associated to both bioregions are observed in winter. In the “High Bloom” bioregion, the deepening of the MLD (when  $MLD > 200$  m) starts in January and ends (when  $MLD < 25$  m) in April, with a very deep MLD observed in February (two mean MLD maxima  $> 880$  m). It should be recalled that MLD estimates are underestimated because profiles are only recorded down to 1000 m, while vertical mixing has been found to reach far greater depths ( $> 2300$  m) in February in the Gulf of Lion [Houpert *et al.*, 2016]. On the contrary, the MLD deepening is shorter and shallower in the “Bloom” bioregion (from February to March only, with a mean MLD maximum  $\sim 475$  m reached within a couple of days only).

The temporal evolutions of  $Z_{0.415}$  and  $Z_{1\%}$  are similar in both bioregions, showing deeper values in summer and autumn, and shallower values during winter/spring (Figure 4d). At the transition periods in autumn and spring, in situ evaluations of  $Z_{1\%}$  and  $Z_{0.415}$  (dark and red points in Figure 4d) are in accordance with the estimates obtained from satellite data (see section 2.3.5). In winter, the shallower  $Z_{1\%}$  and  $Z_{0.415}$  derived from satellite compared to the in situ evaluations could be due to an overestimation of the  $[Chl-a]_{sat}$ , which induced an higher  $K_{PAR}$ . Nevertheless,  $Z_{1\%}$  and  $Z_{0.415}$  show differences in the autumnal shallowing, with a faster shallowing of  $Z_{0.415}$  than  $Z_{1\%}$ , which support the use of  $Z_{0.415}$ , than  $Z_{1\%}$ , in order to not overestimate  $Z_{eu}$ .

The difference in the extent of winter MLD between bioregions can impact phytoplankton retention differently above the  $Z_{eu}$ , defined here as  $Z_{0.415}$ . This impact was addressed through the  $Z_{0.415}/MLD$  ratio (Figure 4e). This ratio can be considered as a proxy of the time when the phytoplankton is mixed below the euphotic zone ( $Z_{0.415}/MLD < 1$ ) or above ( $Z_{0.415}/MLD > 1$ ). A transition period from a  $Z_{0.415}/MLD > 1$  state to a  $Z_{0.415}/MLD < 1$  state (and vice versa) means important changes in light conditions experienced by phytoplankton. In summer, the  $Z_{0.415}/MLD$  ratio is largely greater than 1 ( $Z_{0.415} \gg MLD$ ), whereas it is considerably lesser than 1 in winter ( $Z_{0.415} \ll MLD$ ). Between these two contrasted situations, two transition periods with a MLD close to  $Z_{0.415}$  can be identified ( $Z_{0.415}/MLD \approx 1$ ).

A first transition period occurs in late autumn (early December) in both bioregions. At this time of the year, the MLD deepens in response to an increase in average wind speed and surface heat loss, while the  $Z_{0.415}$  shallows due to the seasonal decrease in  $PAR_0$  (the day length is reduced), and both induced a  $Z_{0.415}/MLD < 1$ . A second transition period occurs in spring (in March). During the spring transition period, the  $Z_{0.415}/MLD$  ratio is highly variable, mostly driven by variations of the mean MLD. After the maximum of MLD that is observed in February, a first event of  $Z_{0.415}/MLD > 1$  occurs. Then a last annual event of very deep MLD is observed in mid-March and can be related to surface heat loss (Figure 4), before the  $Z_{0.415}$  and the MLD come closer again ( $Z_{0.415}/MLD > 1$ ). The temporal dynamics of the  $Z_{0.415}/MLD$  ratio associated with both bioregions, illustrated by color bars (below Figure 4f, with black bars representing  $Z_{0.415}/MLD = 1$ ), are further compared with the observed vertical distribution of [Chl-a] and with the [POC] and  $[NO_3]$  within the MLD.

### 3.3. The MLD, $Z_{0.415}$ , and [Chl-a] Interplay in the Two Bioregions

For the two bioregions, the reconstructed time series of surface [Chl-a] (i.e., [Chl-a] averaged in  $Z_{pd}$ ,  $[Chl-a]_{Z_{pd}}$ ) retrieved from in situ observations (Figure 4f) are similar to those obtained from the  $[Chl-a]_{sat}$ . The low summer and winter  $[Chl-a]_{sat}$  values are confirmed, as well as the delayed and stronger  $[Chl-a]_{sat}$  increase in the “High Bloom.” Then, all [Chl-a] data from the available profiles in both bioregions were averaged every 10 m and every 2 days, in order to describe the vertical distribution of [Chl-a] throughout the annual cycle (Figure 5).

Typical patterns in the vertical distribution of [Chl-a] are associated with the key periods identified thanks to the  $Z_{0.415}/MLD$  ratio. During summer, when the  $Z_{0.415}/MLD$  is greater than 1 ( $Z_{0.415} \gg MLD$ , Figure 5), the vertical distribution of [Chl-a] is characterized by very low surface concentrations ( $[Chl-a] < 0.25$  mg m<sup>-3</sup>) and the presence of a [Chl-a] maximum at depth (DCM), generally above  $Z_{0.415}$ . These summer features in the vertical distribution of [Chl-a] are observed in both bioregions. The [Chl-a] integrated over the  $Z_{0.415}$  ( $[Chl-a]_{Z_{0.415}}$ ) and over 0–1000 m ( $[Chl-a]_{1000}$ ) are similar ( $\sim 25$ – $50$  mg m<sup>-2</sup>, Figure 6).

When the autumnal transition period of the  $Z_{0.415}/MLD$  ratio occurs (in December, Figures 5 and 6), and when the MLD deepens for the first time after the summer, the surface [Chl-a] distribution appears to be homogenous (Figure 5), indicating that the DCM has already vanished (vertical [Chl-a] profiles in Figure 6).

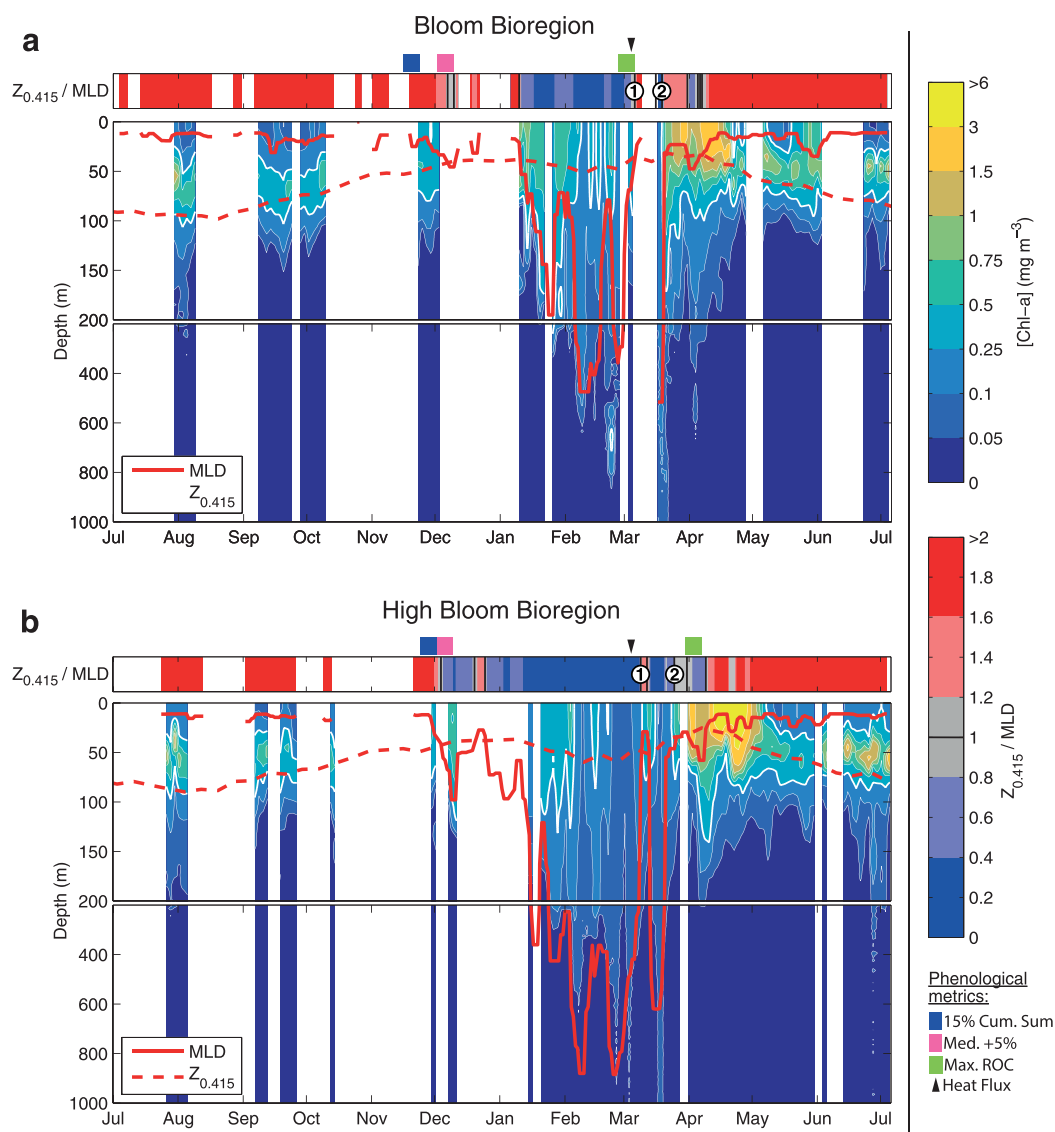


**Figure 5.** Time series of [Chl-a], (a) for the “Bloom” and (b) “High Bloom” bioregions. The color bar for the [Chl-a] applies to both panels (i.e., a and b). The [Chl-a] data have been averaged every 10 m and 2 days. The thickest white line represents the contour line  $0.25 \text{ mg m}^{-3}$ . The solid red line represents the MLD, and the dashed red line the  $Z_{0.415}$ . The color bars above each plot describe the state of the ratio  $Z_{0.415}/\text{MLD}$ , with the phenological metrics from the Figure 2c reported and two spring transition events highlighted (i.e., numbers 1 and 2).

The  $[\text{Chl-a}]_{Z_{0.415}}$  and  $[\text{Chl-a}]_{1000}$  begin to diverge, with the  $[\text{Chl-a}]_{1000}$  increasing more rapidly than the  $[\text{Chl-a}]_{Z_{0.415}}$  (Figure 6).

Thereafter, in winter, the  $Z_{0.415}/\text{MLD}$  ratio is lower than 1 ( $Z_{0.415} \ll \text{MLD}$ , Figure 5). In January, when MLDs are lower than 400 m,  $[\text{Chl-a}]_{1000}$  continues to increase until a maximum in late January ( $\sim 25\text{--}50 \text{ mg m}^{-2}$ , Figure 6). Then, when MLDs reach their maximum with a homogeneous [Chl-a] over the mixed layer, a decrease of the  $[\text{Chl-a}]_{1000}$  is observed in both bioregions ( $\sim 50 \text{ mg m}^{-2}$ ), as well as the annual minimum of  $[\text{Chl-a}]_{Z_{\text{pd}}}$  ( $\sim 0.1 \text{ mg m}^{-3}$  in the “Bloom” bioregion, and  $\sim 0.05 \text{ mg m}^{-3}$  in the “High Bloom” bioregion, Figure 4f) and  $[\text{Chl-a}]_{Z_{0.415}}$  ( $\sim 25 \text{ mg m}^{-2}$  in the “Bloom” bioregion, and  $\sim 11 \text{ mg m}^{-2}$  in the “High Bloom” bioregion, Figure 6). The lowest surface in situ [Chl-a] associated with the “High Bloom” bioregion confirms a higher surface dilution of [Chl-a] in this bioregion, induced by a very deep winter MLD.

At the spring transition period, the MLD becomes lower than  $Z_{0.415}$  and the [Chl-a] increase at the surface (Figures 4–6). The high availability of [Chl-a] profiles in the “High Bloom” bioregion allows a better

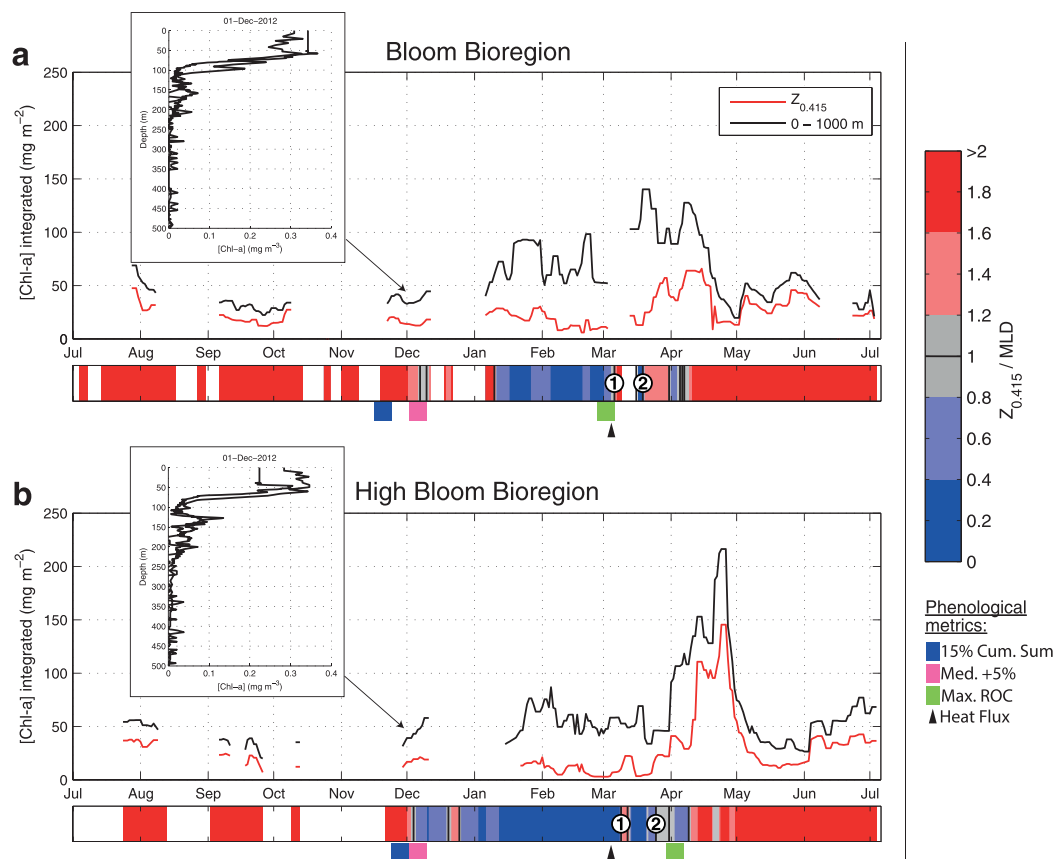


**Figure 6.** Time series of depth integrated [Chl-a], (a) for the “Bloom” and (b) “High Bloom” bioregions. Depth integrations were performed from the surface to  $Z_{0.415}$  (red line) and 1000 m (black line). The values of the [Chl-a] integrated were averaged daily and a 5 day median filter was applied. The color bars below each plot describe the state of the ratio  $Z_{0.415}/MLD$ , with the phenological metrics from the Figure 2c reported and two spring transition events highlighted (i.e., numbers 1 and 2). [Chl-a] profiles realized the 1 December 2012 in the “Bloom” and “High Bloom” bioregions are also reported.

description of the temporal dynamics of such spring [Chl-a] increase, analyzed here with  $r = \partial[\text{Chl-a}]_{Z_{0.415}} / \partial t$  (the growth of the [Chl-a] integrated in  $Z_{0.415}$ ). The MLD becomes shallower than  $Z_{0.415}$  during two successive events: 9 March and 25 March. Each time,  $r$  starts to be positive 1 week before  $Z_{0.415}/MLD > 1$ , and a couple of days before the surface heat flux begins to be positive. Then,  $r$  is maximal at the time of  $Z_{0.415}/MLD > 1$ , or a couple of days before (and 5 or 6 days after the heat flux became positive).

Finally, and in both bioregions, when the  $MLD/Z_{0.415}$  is definitively greater than 1 (i.e., on the 7–9 of April), the maximal annual values of [Chl-a] are observed (Figures 4–6). Note however, that the surface [Chl-a] increase is larger in the “High Bloom” bioregion ( $[\text{Chl-a}]_{Z_{0.415}}$  increased from 25 to 100  $\text{mg m}^{-2}$ , Figure 6b, with higher surface values  $>6 \text{ mg m}^{-3}$ , Figure 5b) than in the “Bloom” bioregion ( $[\text{Chl-a}]_{Z_{0.415}}$  increased from 40 to 70  $\text{mg m}^{-2}$ , Figure 6a, with [Chl-a] surface values  $<3 \text{ mg m}^{-3}$ , Figure 5a).

### 3.4. The $[\text{POC}]_{MLD}$ and $[\text{NO}_3]_{MLD}$ in Both Bioregions

As a reminder, the availability of [POC] and  $[\text{NO}_3]$  profiles is higher after February 2013, thanks to the BGC-Argo floats. Therefore, time series of  $[\text{POC}]_{MLD}$  and of  $[\text{NO}_3]_{MLD}$  were only computed between February 2013 to July 2013. The temporal dynamics of  $[\text{POC}]_{MLD}$  is comparable in both bioregions. In February 2013,  $[\text{POC}]_{MLD}$  is low ( $<30 \text{ mg m}^{-3}$ ). In March and April, during the spring transition period, the  $[\text{POC}]_{MLD}$  increases with surface [Chl-a] (Figure 7). Finally, in summer the  $[\text{POC}]_{MLD}$  decreases, but is still higher than in winter.

From February to early April,  $[\text{NO}_3]_{MLD}$  is generally high with peak values around 8  $\mu\text{M}$  and on average  $\sim 6 \mu\text{M}$  for the “High Bloom” and  $\sim 5 \mu\text{M}$  for the “Bloom” bioregion (Figure 7). High variability around the mean

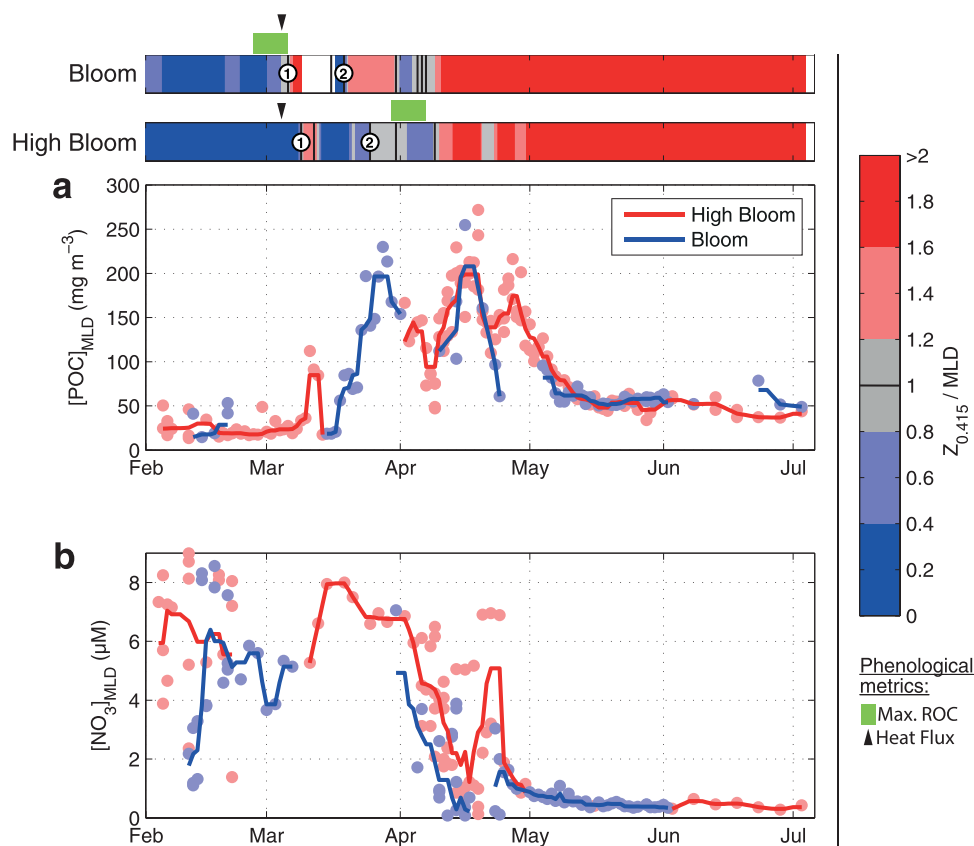


**Figure 7.** Times series of the (a)  $[POC]_{MLD}$  and (b) the  $[NO_3]_{MLD}$  for the “Bloom” (blue) and “High Bloom” (red) bioregions. The lines represent the mean values, median filtered (i.e., 5 days), and the dots the single values. The color bars above the plot describe the state of the  $Z_{0.415}/MLD$  ratio, with the phenological metrics from the Figure 2c reported and two spring transition events highlighted (i.e., numbers 1 and 2).

values is also observed (Figure 7), most probably due to the low availability of  $[NO_3]$  profiles during this period (Figure 3).

Later, from late February to the end of March,  $[NO_3]_{MLD}$  data become scarce, as only a single BGC-Argo float is available for this period. The float initially samples the “Bloom” bioregion measuring  $[NO_3]_{MLD}$  values of  $\sim 4 \mu\text{M}$  and then moves to the “High Bloom” bioregion, where it detects a rapid increase in  $[NO_3]_{MLD}$  from  $\sim 4.5$  to  $8 \mu\text{M}$ . The timing of this nitrate increase coincides with a late mixing event occurring around the 10 March, which deepens the mixed layer down to about 2000 m in the Gulf of Lion [Houpert *et al.*, 2016]. In April,  $[NO_3]_{MLD}$  uniformly decreases in both bioregions. These significant decreases in  $[NO_3]_{MLD}$  are followed by a brief increase in both bioregions (20–23 April), before rapidly and definitely decreasing down to summer values of  $\sim 0.5 \mu\text{M}$  (Figure 7).

#### 4. Discussion

By coupling satellite data with in situ physical and biogeochemical observations, the influence of environmental factors on phytoplankton seasonal cycles in the NWM was analyzed from July 2012 to July 2013. Ocean color data ( $[Chl-a]_{sat}$ ) indicated that surface phytoplankton distribution was structured in two large areas. The later are referred to as the “Bloom” and “High Bloom” bioregions (Figure 2, following the results of Mayot *et al.* [2016]) due to the contrasted timing and intensity of their phytoplankton spring blooms. Using this satellite spatial framework, coherent annual time series of physical and biogeochemical properties associated with these two bioregions were estimated and analyzed.

Mayot *et al.* [2016] demonstrated a relationship between the interannual occurrences in the “High Bloom” bioregion and deep winter convection events. Therefore, a better understanding of the



environmental factors controlling the observed spatial distinction between the “Bloom” and “High Bloom” bioregions will also improve our understanding of the interannual variability in phytoplankton dynamics. In the following sections, we will discuss (1) the processes regulating the temporal dynamics of phytoplankton biomass, with a focus on the autumnal and spring blooms, and (2) the environmental and biological factors inducing differences in phytoplankton biomass between bioregions during the spring bloom.

#### 4.1. The Temporal Dynamics of Phytoplankton in the NWM

For both bioregions, two phenological metrics (i.e., “Heat Flux” and “Max Roc”) identified a spring bloom (in March/April in Figure 2), while two different criteria (i.e., “Med +5%” and “15% Cum”) identified an autumnal bloom. The existence of these two blooms coincides with a typical temperate dynamic.

In temperate seas, the phytoplankton spring bloom is generally thought to begin when the MLD starts to shallow [e.g., Cullen *et al.*, 2002; Chiswell *et al.*, 2015]. This concept was founded on the “critical depth” definition of Sverdrup [1953], the depth at which the vertically integrated phytoplankton production and losses are equal. Stating that a “critical depth” exists, Sverdrup [1953] proposed that the date at which the MLD shallows above this critical depth marks the establishment of the phytoplankton spring bloom. [Chiswell, 2011] demonstrated that the Sverdrup theory could also be used to explain the occurrence of the autumnal bloom, following the definition of an “entrainment bloom” [Cullen *et al.*, 2002]. For the NWM, which lies at the limit between the subtropical and subpolar regimes [Follows and Dutkiewicz, 2001; Henson *et al.*, 2009; Bernardello *et al.*, 2012], the importance of MLD shallowing for spring bloom dynamics has already been mentioned [Lavigne *et al.*, 2013].

However, several recent hypotheses challenged the Sverdrup’s theory, by arguing that the vertical mixing in the mixed layer could be significantly reduced, which allow the onset of blooms in surface and prior to stratification [e.g., Townsend *et al.*, 1994; Huisman *et al.*, 1999; Taylor and Ferrari, 2011a; Franks, 2014]. Similarly, mesoscale features could locally weaken surface turbulence, inducing favorable conditions for bloom onsets [Lévy *et al.*, 1999; Mahadevan *et al.*, 2012]. Another hypothesis is based on trophic interactions within the mixed layer. Behrenfeld [2010] suggested that the phytoplankton biomass accumulation could start in winter when the MLD increase due to the dilution of both phytoplankton and grazers that induce low losses (i.e., “dilution-recoupling model”, see also, Boss and Behrenfeld [2010] and Behrenfeld and Boss [2014]).

In our study, the autumnal and spring bloom periods were unambiguously identified by changes in the  $Z_{0.415}$ /MLD ratio. Therefore, in the next section, we will focus on the environmental and biological factors controlling the link between the  $Z_{0.415}$ /MLD ratio and the phytoplankton bloom periods, by accounting for the above mentioned theories.

##### 4.1.1. The Autumnal Bloom to the Winter Period

In autumn, the  $Z_{0.415}$  and MLD interfaces overlapped, with a  $Z_{0.415}$ /MLD < 1 in both bioregions (in November/December, Figure 4). This transition period was associated with the surface autumnal increase in [Chl-a] (i.e., [Chl-a]<sub>sat</sub> and [Chl-a]<sub>Z<sub>pd</sub></sub>) and an homogenous vertical distribution of [Chl-a] (Figure 6). A couple of months before (in September/October), the vertical distribution of [Chl-a] was on the contrary characterized by a DCM (Figure 5). The surface increase in [Chl-a] was likely related to a change in the vertical distribution of the phytoplankton. Such modification could be due to a progressive reduction of the DCM and a redistribution of the phytoplankton biomass over a more uniform shape [Morel and André, 1991; Lavigne *et al.*, 2015a].

Whatever the bioregion, our data indicated that the DCM progressively shallows in late summer/autumn following the  $Z_{0.415}$  interface (Figure 5), thus suggesting a light-driven control of the [Chl-a] vertical distribution [Mignot *et al.*, 2014; Lavigne *et al.*, 2015a]. To support such DCM shallowing, a rise in the nitracline would also be required. During this season, the intensification of the large-scale cyclonic circulation over the whole NWM actually uplifted the nitracline [Pasquero de Fommervault *et al.*, 2015a]. Then, the slight autumnal deepening of the MLD leads to the mixing-up of the top layer of the summer shallowing DCM. This autumnal MLD deepening was related to processes affecting the vertical mixing at this season: water column stratification, the integrated effects of air-sea fluxes, and advection processes (as discussed for the 2012–2013 particular year in Estournel *et al.* [2016], Houpert *et al.* [2016], and Waldman *et al.* [2017]).

The surface [Chl-a] increase in autumn lasted until the end of January. The [Chl-a] integrated between 0 and 1000 m also increased. Assuming that [Chl-a] is a proxy for phytoplankton biomass, and following the “critical-depth theory” of Sverdrup, this suggests the MLD did not reach the critical depth. Conversely, the shallowing of the nitracline and the concomitant deepening of the MLD could induce an effective injection of nitrates into the surface layers and the development of a typical “entrainment bloom” [Cullen *et al.*, 2002; Chiswell, 2011]. Consequently, the autumnal increase in [Chl-a] that is recurrently observed in the NWM [Morel and André, 1991; Volpe *et al.*, 2012; D’Ortenzio *et al.*, 2014] could be an effective biomass increase.

However, during this period,  $PAR_0$  level was low and could have led to reduced light availability in the MLD, in conjunction with the later’s deepening. Both of these environmental factors may have induced an intracellular increase of [Chl-a] in the phytoplankton cells due to the photoacclimation (a low carbon to chlorophyll ratio, Behrenfeld *et al.* [2005]), and could explain a part of the observed autumnal [Chl-a] increase [Mignot *et al.*, 2014]. This suggests that the increase in surface [Chl-a] in November/December probably does not reveal an effective increase in the phytoplankton biomass. Unfortunately, simultaneous in situ data of [Chl-a] and  $b_{bp}$  were unavailable at this period of the year, thus preventing us from evaluating the photoacclimation processes (like in Mignot *et al.* [2014]).

Then, during the very deep winter MLD period, the  $[Chl-a]_{1000}$  decreased in both bioregions. This suggests that the winter integrated losses of phytoplankton biomass over the water column exceeded the integrated phytoplankton production. In addition, in winter, there was no trend toward an increase in the  $[Chl-a]_{1000}$ , which suggests that, contrary to the “decoupling-recoupling model” of Behrenfeld [2010], and results obtained by model simulations [Herrmann *et al.*, 2013], the deep winter MLDs do not induce a positive net increase of the phytoplankton biomass.

#### 4.1.2. The Spring Bloom Temporal Dynamics

The spring transition period, coincided with the strongest annual increase in [Chl-a]. The availability of in situ data in the “High Bloom” bioregion allows to investigate the environmental factors that may explain this relationship.

During the winter to spring transition, two successive events of surface [Chl-a] increase were identified and separated by a 1 week period of strong MLD deepening. The last mixing event in mid-March was well identified with in situ data and described as a late deep mixing event that occurred this year in the NWM [Houpert *et al.*, 2016]. Nevertheless, the temporal dynamics of the [Chl-a] increase were similar during these two successive events and were typical of a temperate spring bloom.

At the beginning of each of the two spring bloom transition periods, the MLD remained deep but the mixed layer might not be actively mixing [Townsend *et al.*, 1994; Chiswell, 2011; Taylor and Ferrari, 2011b; Franks, 2014]. [Taylor and Ferrari, 2011b] supposed that after the winter mixing period, lowered vertical mixing occurs mainly at the surface and is caused by the reduction of net surface heat loss by the ocean. According to the authors, the spring bloom should initiate when the heat flux becomes positive. In our case, the [Chl-a] started to increase in surface only two days before the surface heat flux became positive. Therefore, the hypothesis of a reduction of the mixing in surface due to net heat gains could be relevant, although buoyancy gain by horizontal processes may be important for the deep convection process of the NWM [Estournel *et al.*, 2016].

One week later, the MLD overlapped with  $Z_{0.415}$  ( $Z_{0.415}/MLD > 1$ ) and the increase in the [Chl-a] integrated over the  $Z_{0.415}$  was maximal. Assuming that  $Z_{0.415}$  is a good proxy for the  $Z_{eu}$ , this depth also represents the equivalent depth, where the instantaneous production and losses are equal [Sverdrup, 1953]. Therefore, when  $Z_{0.415}/MLD > 1$ , the integrated phytoplankton production in the  $Z_{0.415}$  should largely overcome the integrated losses. Using a dedicated model, [Llort *et al.*, 2015] demonstrated that the maximal annual increase in phytoplankton production occurs during the spring restratification, and they attributed this maximal annual increase to a change in the light condition. Here we showed that during the spring transition period, the surface [Chl-a] (i.e.,  $[Chl-a]_{Z_{0.415}}$ ) corresponds to an increase in the phytoplankton production (since it is simultaneous with the spring increase of [POC]) and that its maximal increase is related to a change in the light condition since the  $Z_{0.415}/MLD$  ratio became  $>1$  (a large part of the phytoplankton remain in the  $Z_{eu}$ ).

However, the autumnal mixing as well as the spring restratification are not monotonous processes. In both bioregions, the  $Z_{0.415}/\text{MLD}$  were indeed characterized by an important variability, oscillating between values  $<1$  and  $>1$  with 3 week intervals, from December to March (Figure 4e). These observations highlight that, during these critical transition periods, subseasonal processes influence both the mixing and the restratification of the water column and therefore the response of phytoplankton [Franks, 2014; Thomalla et al., 2015]. Similar conclusions were obtained by model simulations [Bernardello et al., 2012]. However, it is noteworthy that our analysis was conducted over large areas (i.e., bioregions) in order to identify key environmental factors influencing the phytoplankton blooms, and did not focus on the smaller scale processes that could obviously influence phytoplankton growth [Franks, 2014].

#### 4.2. The Spring Bloom Magnitude

After the 9 April, the water column was definitely stratified in both bioregions ( $Z_{0.415}/\text{MLD} > 1$ , Figure 4e). At that time, most of the phytoplankton biomass was concentrated in the  $Z_{0.415}$  layer (Figure 5). However, bioregions displayed different spring bloom intensities. In the “High bloom” bioregion, higher surface values ( $>6 \text{ mg m}^{-3}$ , Figure 5) than in the “Bloom” bioregion (surface values  $< 3 \text{ mg m}^{-3}$ , Figure 5) were found, and were in the range of values previously reported for the NWM [Conan et al., 1999; Estrada and Vaqué, 2014]. This suggests higher surface net accumulation rates (more gains than losses) of phytoplankton in the “High Bloom” bioregion than in the “Bloom” bioregion.

Differences in phytoplankton community composition, which influence the net accumulation rate of phytoplankton biomass, could explain the observed difference in the [Chl-a] magnitude within bioregions. Diatoms are characterized by a higher maximal growth rate than the smaller phytoplankton species, and higher light levels requirements [Edwards et al., 2015]. They generally dominate the phytoplankton spring bloom community in March–April [Marty et al., 2002; Siokou-Frangou et al., 2010; Estrada and Vaqué, 2014; Thyssen et al., 2014; Romagnan et al., 2015; Mayot et al., 2017]. However, the relative abundance of diatoms within the phytoplankton spring bloom community exhibited strong interannual variability in the NWM [Organelli et al., 2013]. High concentrations of diatoms were observed after strong winter mixing events [Estrada et al., 1999; Marty et al., 2002; Rigual-Hernández et al., 2013; Mayot et al., 2017]. Therefore, a stronger accumulation of diatoms in the “High Bloom” bioregion rather than in the “Bloom” bioregion could explain the differences in the net accumulation rate of phytoplankton biomass. As a matter of fact, Mayot et al., [2017] found a higher proportion of diatoms in the phytoplankton community in the “High Bloom” bioregion ( $\sim 48\%$ ) than in the “Bloom” bioregion ( $\sim 36\%$ ), from the DEWEX ship survey stations performed in April 2013.

The higher diatom concentration could be explained by a change in silicates surface availability that was induced by strong winter mixing [Severin et al., 2014]. Therefore, we suggest that the difference in net phytoplankton accumulation rates cannot be ascribed to higher nitrates surface availability in the “High Bloom” bioregion. Indeed,  $[\text{NO}_3]_{\text{MLD}}$  were quite constant since the end of winter (Figure 7) and more importantly, they were particularly high ( $>6 \mu\text{M}$ ) compared to the rest of the Mediterranean basin [Pujo-Pay et al., 2011]. In the NWM, the nitracline is generally close to the surface [Pasqueron de Fommervault et al., 2015a, 2015b], in association with the thermocline [Diaz et al., 2000; Pujo-Pay et al., 2011], and can be reached by a relatively shallow MLD [D’Ortenzio et al., 2014]. In addition, nitrates concentration sharply increases in subsurface waters [Pasqueron de Fommervault et al., 2015b] (Figure 8a). In other terms, although maximum winter MLDs were very different between both bioregions (Figure 4c), the  $[\text{NO}_3]$  that is available for the next spring should remain similar in both areas.

On the contrary, silicates concentration in the NWM progressively increases downward from the surface [Pasqueron de Fommervault et al., 2015b] (Figure 8b). Deep winter convection events which reach the deep water masses are necessary to strongly increase the surface availability of silicates for the coming spring bloom. Thus, the stronger and longer winter mixing in the “High Bloom” bioregion could have enhanced silicates availability, generating more favorable conditions for diatoms, and leading to the development of an enhanced diatom spring bloom. Severin et al. [2017] showed that the DEWEX ship surveys stations performed in February 2013 inside the deep convection area presented higher surface  $[\text{Si}(\text{OH})_4]$  and higher silicates to nitrates (Si:N) ratio ( $[\text{Si}(\text{OH})_4] \sim 7.1 \mu\text{M}$  and Si:N  $\sim 0.86$ ) than the ship surveys stations performed in the surrounding mixed area ( $[\text{Si}(\text{OH})_4] \sim 3.63 \mu\text{M}$  and Si:N  $\sim 0.70$ ).

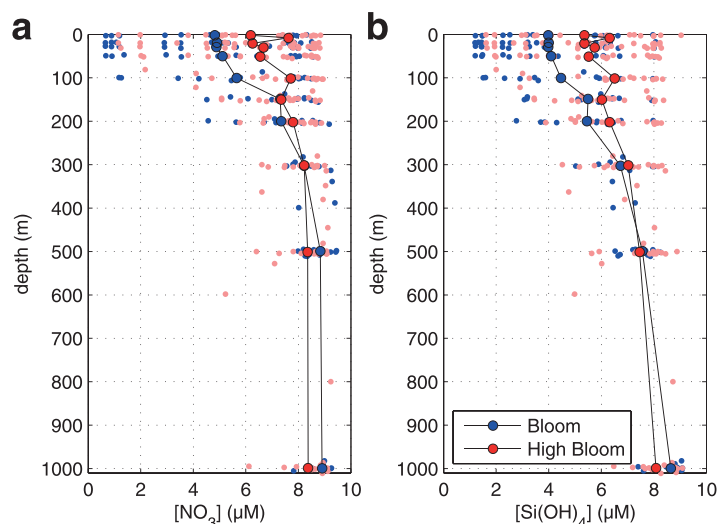


**Figure 8.** Mean profiles of (a)  $[\text{NO}_3^-]$  and (b)  $[\text{Si}(\text{OH})_4]$  in February 2013 in the “Bloom” (blue) and “High Bloom” (red) bioregions. The lines represent the mean values and the dots the single values.

## 5. Conclusion

The main objective of this study was to understand the influence of the physical and biogeochemical properties driving the phytoplankton annual cycle in the temperate regime of the NWM. An unprecedented sampling effort was carried out over a year from July 2012 to July 2013 and coupled data from several platforms. Combined with a satellite-based bioregionalization, an exceptional dataset was collected in terms of number of profiles and parameters (both physical and biogeochemical). Therefore, an analysis with in situ data of the primary drivers of the phytoplankton

blooms was made possible over a complete annual cycle and not, as usual, restricted to a short period or area.

During the year 2012–2013, ocean color observations, supported by in situ measurements, revealed the existence of two large-scale areas (or bioregions) bearing similar phytoplankton autumnal blooms but contrasted spring blooms. The timing of the bloom events identified by existing methods (mostly based on remotely sensed ocean color data) confirmed the temperate nature of the NWM area with both autumnal and spring blooms. However, the use of these phenological metrics only provided a partial vision of the phytoplankton annual cycle. The  $Z_{0.415}/\text{MLD}$  ratio, by inferring the time when the phytoplankton is mixed below or above the euphotic zone, provided an accurate alternative to detect the dates of the main bloom events in the NWM.

The phytoplankton autumnal bloom, that occurs when  $Z_{0.415}/\text{MLD}$  ratio changes from  $>1$  to  $<1$ , is likely explained by overlapping processes, related to the erosion of the summer water column stratification and light availability. In fact, the deepening of the MLD and the light driven displacement to the surface of the DCM may have induced a redistribution of the  $[\text{Chl-a}]$  within the surface layer. The MLD deepening could also have injected nutrients into the surface layer thus sustaining phytoplankton growth, while the reduced light availability at this season should also generate  $[\text{Chl-a}]$  increases through photoacclimation. In spring, the  $Z_{0.415}/\text{MLD}$  ratio becomes  $>1$  again and is related to the timing of the highest accumulation rate of phytoplankton biomass, while the spring bloom onset appears more related to a less intense mixing in surface winter mixed layer.

Finally, our analysis evidenced an unusually high net accumulation rate of phytoplankton biomass in spring where winter deep water convection events had occurred. However, the winter availability of nitrate in the surface layer was homogeneously high over the whole NWM (not restricted to the deep convection area), suggesting that a higher availability of nitrate can probably not explain the unusually high spring phytoplankton biomass. Instead, we suggest that very deep winter MLD lead to an increased silicates availability in the surface, which could also explain the dominance of diatoms in the underpinning spring phytoplankton community, as well as the unusually high accumulation rates of phytoplankton.

The results obtained in the NWM provide a new framework to characterize the phytoplankton seasonality in temperate seas (i.e., oceanic regions submitted to strong seasonality). The combined use of satellites, ship-based sampling and mainly in situ autonomous platforms (i.e., Argo and BGC-Argo floats, and biological gliders) allowed us to retrieve physical and biogeochemical properties along the water column, and to enhance our interpretation of the physical-biological coupling in the NWM.



**Acknowledgments**

The authors would like to thank the NASA Ocean Biology Processing Group (OBPG) for the access to MODIS data (<http://oceancolor.gsfc.nasa.gov>). The Argo-floats data were collected and made freely available by the Coriolis project and programs that contribute to it (<http://www.coriolis.eu.org>). Bio-Argo float data used in this work are made available online ([http://www.oao.obs-vlfr.fr/BD\\_FLOAT/NETCDF/](http://www.oao.obs-vlfr.fr/BD_FLOAT/NETCDF/)). This work is a contribution to the MerMEx project (Marine Ecosystem Response in the Mediterranean Experiment, WP1) from the MISTRALS international program. This work was supported by the remOcean (remotely sensed biogeochemical cycles in the Ocean) project, funded by the European Research Council (GA 246777), by the French "Equipement d'avenir" NAOs project (ANR J11R107-F), and by the PACA region. The authors are also grateful to the French Bio-Argo project funded by CNES-TOSCA, and to LEFE Cyber and GMMC programs that supported this work. We also thank F. Benedetti for reviewing the manuscript. Finally, we are grateful to two anonymous reviewers for their valuable comments and suggestions.

**References**

Alberola, C., C. Millot, and J. Font (1995), On the seasonal and mesoscale variabilities of the Northern Current during the PRIMO-0 experiment in the western Mediterranean-sea, *Oceanol. Acta*, *18*(2), 163–192.

Aminot, A., and R. K erouel (2007), *Dosage automatique des nutriments dans les eaux marines: m ethodes en flux continu*, Editions Quae, IFREMER, Versailles, France.

Barale, V., J.-M. Jaquet, and M. Ndiaye (2008), Algal blooming patterns and anomalies in the Mediterranean Sea as derived from the SeaWiFS data set (1998–2003), *Remote Sens. Environ.*, *112*(8), 3300–3313, doi:10.1016/j.rse.2007.10.014.

Barnard, A. H., and T. O. Mitchell (2013), Biogeochemical monitoring of the oceans using autonomous profiling floats, *Ocean News Technol.*, *19*(2), 16–17.

Behrenfeld, M. J. (2010), Abandoning Sverdrup’s critical depth hypothesis on phytoplankton blooms, *Ecology*, *91*(4), 977–989.

Behrenfeld, M. J., and E. S. Boss (2014), Resurrecting the ecological underpinnings of ocean plankton blooms, *Ann. Rev. Mar. Sci.*, *6*(1), 167–194, doi:10.1146/annurev-marine-052913-021325.

Behrenfeld, M. J., E. S. Boss, D. A. Siegel, and D. M. Shea (2005), Carbon based ocean productivity and phytoplankton physiology from space, *Global Biogeochem. Cycles*, *19*, GB1006, doi:10.1029/2004GB002299.

Bernardello, R., J. G. Cardoso, N. Bahamon, D. Donis, I. Marinov, and A. Cruzado (2012), Factors controlling interannual variability of vertical organic matter export and phytoplankton bloom dynamics—a numerical case-study for the NW Mediterranean Sea, *Biogeosciences*, *9*(11), 4233–4245, doi:10.5194/bg-9-4233-2012.

Biogeochemical-Argo Planning Group (2016), *The Scientific Rationale, Design and Implementation Plan for a Biogeochemical-Argo Float Array*, Ifremer, France.

Bosc, E., A. Bricaud, and D. Antoine (2004), Seasonal and interannual variability in algal biomass and primary production in the Mediterranean Sea, as derived from 4 years of SeaWiFS observations, *Global Biogeochem. Cycles*, *18*, GB1005, doi:10.1029/2003GB002034.

Boss, E., and M. Behrenfeld (2010), In situ evaluation of the initiation of the North Atlantic phytoplankton bloom, *Geophys. Res. Lett.*, *37*, L18603, doi:10.1029/2010GL044174.

Bosse, A., P. Testor, L. Mortier, L. Prieur, V. Taillandier, F. d’Ortenzio, and L. Coppola (2015), Spreading of Levantine Intermediate Waters by submesoscale coherent vortices in the northwestern Mediterranean Sea as observed with gliders, *J. Geophys. Res. Oceans*, *120*, 1599–1622, doi:10.1002/2014JC010263.

Briggs, N., M. J. Perry, I. Cetinić, C. Lee, E. D’Asaro, A. M. Gray, and E. Rehm (2011), High-resolution observations of aggregate flux during a sub-polar North Atlantic spring bloom, *Deep Sea Res., Part I*, *58*(10), 1031–1039, doi:10.1016/j.dsr.2011.07.007.

Brody, S. R., and M. S. Lozier (2014), Changes in dominant mixing length scales as a driver of subpolar phytoplankton bloom initiation in the North Atlantic, *Geophys. Res. Lett.*, *41*, 3197–3203, doi:10.1002/2014GL059707.

Brody, S. R., M. S. Lozier, and J. P. Dunne (2013), A comparison of methods to determine phytoplankton bloom initiation, *J. Geophys. Res. Oceans*, *118*, 2345–2357, doi:10.1002/jgrc.20167.

Cetinić, I., M. Perry, N. Briggs, and E. Kallin (2012), Particulate organic carbon and inherent optical properties during 2008 North Atlantic Bloom Experiment, *J. Geophys. Res.*, *117*, C06028, doi:10.1029/2011JC007771.

Cetinić, I., M. J. Perry, E. D’Asaro, N. Briggs, N. Poulton, M. E. Sieracki, and C. M. Lee (2015), A simple optical index shows spatial and temporal heterogeneity in phytoplankton community composition during the 2008 North Atlantic Bloom Experiment, *Biogeosciences*, *12*(7), 2179–2194.

Chiswell, S. M. (2011), Annual cycles and spring blooms in phytoplankton: Don’t abandon Sverdrup completely, *Mar. Ecol. Prog. Ser.*, *443*, 39–50.

Chiswell, S. M., P. H. R. Calil, and P. W. Boyd (2015), Spring blooms and annual cycles of phytoplankton: A unified perspective, *J. Plankton Res.*, *37*(3), 500–508.

Conan, P., C. Turley, E. Stutt, M. Pujo-Pay, and F. Van Wambeke (1999), Relationship between phytoplankton efficiency and the proportion of bacterial production to primary production in the Mediterranean Sea, *Aquat. Microb. Ecol.*, *17*(2), 131–144.

Cullen, J. J., P. J. S. Franks, D. M. Karl, and A. Longhurst (2002), Physical influences on marine ecosystem dynamics, *Sea*, *12*, 297–336.

D’Ortenzio, F., and M. Ribera d’Alcal  (2009), On the trophic regimes of the Mediterranean Sea: A satellite analysis, *Biogeosciences*, *6*(2), 139–148, doi:10.5194/bg-6-139-2009.

D’Ortenzio, F., D. Iudicone, C. de Boyer Montegut, P. Testor, D. Antoine, S. Marullo, R. Santoleri, and G. Madec (2005), Seasonal variability of the mixed layer depth in the Mediterranean Sea as derived from in situ profiles, *Geophys. Res. Lett.*, *32*, L12605, doi:10.1029/2005GL022463.

D’Ortenzio, F., S. Le Reste, H. Lavigne, F. Besson, H. Claustre, L. Coppola, A. Dufour, V. Dutreuil, A. Laes, and E. Leymarie (2012), Autonomously profiling the nitrate concentrations in the ocean: The Pronuts project, *Mercat. Ocean. Q. Newsl.*, *45*, 8–11.

D’Ortenzio, F., H. Lavigne, F. Besson, H. Claustre, L. Coppola, N. Garcia, A. La s-Huon, S. Le Reste, D. Malard , and C. Migon (2014), Observing mixed layer depth, nitrate and chlorophyll concentrations in the northwestern Mediterranean: A combined satellite and NO<sub>3</sub> profiling floats experiment, *Geophys. Res. Lett.*, *41*, 6443–6451, doi:10.1002/2014GL061020.

Dee, D. P., S. M. Uppala, A. J. Simmons, P. Berrisford, P. Poli, S. Kobayashi, U. Andrae, M. A. Balmaseda, G. Balsamo, and P. Bauer (2011), The ERA Interim reanalysis: Configuration and performance of the data assimilation system, *Q. J. R. Meteorol. Soc.*, *137*(656), 553–597.

Devred, E., S. Sathyendranath, and T. Platt (2007), Delineation of ecological provinces using ocean colour radiometry, *Mar. Ecol. Prog. Ser.*, *346*, 1–13.

Diaz, F., P. Raimbault, and P. Conan (2000), Small-scale study of primary productivity during spring in a Mediterranean coastal area (Gulf of Lions), *Cont. Shelf Res.*, *20*(9), 975–996.

Donlon, C. J., M. Martin, J. Stark, J. Roberts-Jones, E. Fiedler, and W. Wimmer (2012), The operational sea surface temperature and sea ice analysis (OSTIA) system, *Remote Sens. Environ.*, *116*, 140–158.

Edwards, K. F., M. K. Thomas, C. A. Klausmeier, and E. Litchman (2015), Light and growth in marine phytoplankton: Allometric, taxonomic, and environmental variation, *Limnol. Oceanogr., Methods*, *60*(2), 540–552.

Estournel, C., et al. (2016), High resolution modeling of dense water formation in the north-western Mediterranean during winter 2012–2013: Processes and budget, *J. Geophys. Res. Oceans*, *121*, 5367–5392, doi:10.1002/2016JC011935.

Estrada, M., and D. Vaqu  (2014), Microbial components, in *The Mediterranean Sea*, edited by S. Goffredo and Z. Dubinsky, pp. 87–111, Springer, Berlin.

Estrada, M., R. A. Varela, J. Salat, A. Cruzado, and E. Arias (1999), Spatio-temporal variability of the winter phytoplankton distribution across the Catalan and North Balearic fronts(NW Mediterranean), *J. Plankton Res.*, *21*(1), 1–20.



- Estrada, M., M. Latasa, M. Emelianov, A. Gutiérrez-Rodríguez, B. Fernández-Castro, J. Isern-Fontanet, B. Mouriño-Carballido, J. Salat, and M. Vidal (2014), Seasonal and mesoscale variability of primary production in the deep winter-mixing region of the NW Mediterranean, *Deep Sea Res., Part I*, *94*, 45–61.
- Ferreira, A. S., A. W. Visser, B. R. MacKenzie, and M. R. Payne (2014), Accuracy and precision in the calculation of phenology metrics, *J. Geophys. Res. Oceans*, *119*, 8438–8453, doi:10.1002/2014JC010323.
- Ferrari, R., S. T. Merrifield, and J. R. Taylor (2015), Shutdown of convection triggers increase of surface chlorophyll, *J. Mar. Syst.*, *147*, 116–122.
- Follows, M., and S. Dutkiewicz (2001), Meteorological modulation of the North Atlantic spring bloom, *Deep Sea Res., Part II*, *49*(1), 321–344.
- Font, J., E. Garcia Ladona, and E. Gorriz (1995), The seasonality of mesoscale motion in the northern current of the western mediterranean—Several years of evidence, *Oceanol. Acta*, *18*(2), 207–219.
- Frajka-Williams, E., and P. B. Rhines (2010), Physical controls and interannual variability of the Labrador Sea spring phytoplankton bloom in distinct regions, *Deep Sea Res., Part I*, *57*(4), 541–552.
- Franks, P. J. S. (2014), Has Sverdrup's critical depth hypothesis been tested? Mixed layers vs. turbulent layers, *ICES J. Mar. Sci.*, *72*(6), 1897–1907, doi:10.1093/icesjms/fsu175.
- Gordon, H. R., and W. R. McCluney (1975), Estimation of the depth of sunlight penetration in the sea for remote sensing, *Appl. Opt.*, *14*(2), 413–416.
- Henson, S. A., J. P. Dunne, and J. L. Sarmiento (2009), Decadal variability in North Atlantic phytoplankton blooms, *J. Geophys. Res. Oceans*, *114*, C04013, doi:10.1029/2008JC005139.
- Herrmann, M., F. Diaz, C. Estournel, P. Marsaleix, and C. Ulse (2013), Impact of atmospheric and oceanic interannual variability on the Northwestern Mediterranean Sea pelagic planktonic ecosystem and associated carbon cycle, *J. Geophys. Res. Oceans*, *118*, 5792–5813, doi:10.1002/jgrc.20405.
- Hopkins, J., S. A. Henson, S. C. Painter, T. Tyrrell, and A. J. Poulton (2015), Phenological characteristics of global coccolithophore blooms, *Global Biogeochem. Cycles*, *29*(2), 239–253.
- Houpert, L., P. Testor, X. D. de Madron, S. Somot, F. D'Ortenzio, C. Estournel, and H. Lavigne (2014), Seasonal cycle of the mixed layer, the seasonal thermocline and the upper-ocean heat storage rate in the Mediterranean Sea derived from observations, *Prog. Oceanogr.*, *132*, 333–352, doi:10.1016/j.pocean.2014.11.004.
- Houpert, L., et al. (2016), Observations of open-ocean deep convection in the northwestern Mediterranean Sea: Seasonal and interannual variability of mixing and deep water masses for the 2007–2013 period, *J. Geophys. Res. Oceans*, *121*, 8139–8171, doi:10.1002/2016JC011857.
- Huisman, J., P. van Oostveen, and F. J. Weissing (1999), Critical depth and critical turbulence: Two different mechanisms for the development of phytoplankton blooms, *Limnol. Oceanogr.*, *44*(7), 1781–1787.
- Johnson, K. S., and L. J. Coletti (2002), In situ ultraviolet spectrophotometry for high resolution and long-term monitoring of nitrate, bromide and bisulfide in the ocean, *Deep Sea Res., Part I*, *49*(7), 1291–1305.
- Lacour, L., H. Claustre, L. Prieur, and F. D'Ortenzio (2015), Phytoplankton biomass cycles in the North Atlantic subpolar gyre: A similar mechanism for two different blooms in the Labrador Sea, *Geophys. Res. Lett.*, *42*, 5403–5410, doi:10.1002/2015GL064540.
- Lavigne, H., F. D'Ortenzio, H. Claustre, and A. Poteau (2012), Towards a merged satellite and in situ fluorescence ocean chlorophyll product, *Biogeosciences*, *9*(6), 2111–2125.
- Lavigne, H., F. D'Ortenzio, C. Migon, H. Claustre, P. Testor, M. R. d'Alcala, R. Lavezza, L. Houpert, and L. Prieur (2013), Enhancing the comprehension of mixed layer depth control on the Mediterranean phytoplankton phenology, *J. Geophys. Res. Oceans*, *118*, 3416–3430, doi:10.1002/jgrc.20251.
- Lavigne, H., F. D'Ortenzio, M. Ribera D'Alcalà, H. Claustre, R. Sauzède, and M. Gacic (2015a), On the vertical distribution of the chlorophyll a concentration in the Mediterranean Sea: A basin-scale and seasonal approach, *Biogeosciences*, *12*(16), 5021–5039, doi:10.5194/bg-12-5021-2015.
- Lavigne, H., F. D'Ortenzio, M. Ribera D'Alcalà, H. Claustre, R. Sauzède, and M. Gacic (2015b), On the vertical distribution of the chlorophyll a concentration in the Mediterranean Sea: A basin-scale and seasonal approach, *Biogeosciences*, *12*(16), 5021–5039.
- Le Traon, P.-Y., F. D'Ortenzio, M. Babin, H. Claustre, S. Pouliquen, S. Le Reste, V. Thierry, P. Brault, M. Guigue, and M. Le Menn (2012), NAOS: Preparing the new decade for Argo, *Mercat. Ocean. Q. Newsl.*, *45*, 3–4.
- Letelier, R. M., D. M. Karl, M. R. Abbott, and R. R. Bidigare (2004), Light driven seasonal patterns of chlorophyll and nitrate in the lower euphotic zone of the North Pacific Subtropical Gyre, *Limnol. Oceanogr.*, *49*(2), 508–519.
- Lévy, M., L. Mémary, and G. Madec (1998), The onset of a bloom after deep winter convection in the northwestern Mediterranean sea: Mesoscale process study with a primitive equation model, *J. Mar. Syst.*, *16*(1), 7–21.
- Lévy, M., L. Mémary, and G. Madec (1999), The onset of the spring bloom in the MEDOC area: Mesoscale spatial variability, *Deep Sea Res., Part I*, *46*(7), 1137–1160.
- Llort, J., M. Lévy, J.-B. Sallée, and A. Tagliabue (2015), Onset, intensification, and decline of phytoplankton blooms in the Southern Ocean, *ICES J. Mar. Sci.*, *72*(6), 1971–1984, doi:10.1093/icesjms/fsv053.
- Loisel, H., E. Bose, D. Stramski, and K. Oubelkheir (2001), Seasonal variability of the backscattering coefficient in the Mediterranean Sea based on Satellite SeaWiFS imagery, *Geophys. Res. Lett.*, *28*, 4203–4206.
- Mahadevan, A., E. D'Asaro, C. Lee, and M. J. Perry (2012), Eddy-driven stratification initiates North Atlantic spring phytoplankton blooms, *Science*, *337*(6090), 54–58.
- Marshall, J., and F. Schott (1999), Open ocean convection: Observations, theory, and models, *Rev. Geophys.*, *37*(1), 1–64, doi:10.1029/98RG02739.
- Marty, J., and J. Chiavérini (2002), Seasonal and interannual variations in phytoplankton production at DYFAMED time-series station, northwestern Mediterranean Sea, *Deep Sea Res., Part II*, *49*, 2017–2030.
- Marty, J.-C., J. Chiavérini, M.-D. Pizay, and B. Avril (2002), Seasonal and interannual dynamics of nutrients and phytoplankton pigments in the western Mediterranean Sea at the DYFAMED time-series station (1991–1999), *Deep Sea Res., Part II*, *49*(11), 1965–1985, doi:10.1016/S0967-0645(02)00022-X.
- Marty, J. C., and J. Chiavérini (2010), Hydrological changes in the Ligurian Sea (NW Mediterranean, DYFAMED site) during 1995–2007 and biogeochemical consequences, *Biogeosciences*, *7*(7), 2117–2128.
- Mayot, N., F. D'Ortenzio, M. Ribera d'Alcalà, H. Lavigne, and H. Claustre (2016), Interannual variability of the Mediterranean trophic regimes from ocean color satellites, *Biogeosciences*, *13*, 1901–1917.
- Mayot, N., et al. (2017), Influence of the phytoplankton community structure on the spring and annual primary production in the North-Western Mediterranean Sea, *J. Geophys. Res. Oceans.*, doi:10.1002/2016JC012668, in press.
- MEDOC Group (1970), Observation of formation of deep water in the Mediterranean Sea, 1969, *Nature*, *227*(5262), 1037–1040, doi:10.1038/2271037a0.

- Mignot, A., H. Claustre, J. Uitz, A. Poteau, F. D'Ortenzio, and X. Xing (2014), Understanding the seasonal dynamics of phytoplankton biomass and the deep chlorophyll maximum in oligotrophic environments: A Bio-Argo float investigation, *Global Biogeochem. Cycles*, 28(8), 856–876.
- Millot, C. (1999), Circulation in the Western Mediterranean Sea, *J. Mar. Syst.*, 20(1), 423–442, doi:10.1016/S0924-7963(98)00078-5.
- Mobley, C. D., and E. S. Boss (2012), Improved irradiances for use in ocean heating, primary production, and photo-oxidation calculations, *Appl. Opt.*, 51(27), 6549–6560.
- Morel, A., and J. M. André (1991), Pigment distribution and primary production in the western Mediterranean as derived and modeled from Coastal Zone Color Scanner observations, *J. Geophys. Res.*, 96, 12,685–12,698, doi:10.1029/91JC00788.
- Morel, A., and J. F. Berthon (1989), Surface pigments, algal biomass profiles, and potential production of the euphotic layer: Relationships reinvestigated in view of remote-sensing applications, *Limnol. Oceanogr.*, 34(8), 1545–1562.
- Morel, A., Y. Huot, B. Gentili, P. J. Werdell, S. B. Hooker, and B. A. Franz (2007), Examining the consistency of products derived from various ocean color sensors in open ocean (Case 1) waters in the perspective of a multi-sensor approach, *Remote Sens. Environ.*, 111(1), 69–88.
- Niewiadomska, K., H. Claustre, L. Prieur, and F. d'Ortenzio (2008), Submesoscale physical-biogeochemical coupling across the Ligurian current (northwestern Mediterranean) using a bio-optical glider, *Limnol. Oceanogr. Methods*, 53(5), 2210.
- Olita, A., A. Ribotti, R. Sorgente, L. Fazioli, and A. Perilli (2011), SLA-chlorophyll-a variability and covariability in the Algero-Provençal Basin (1997–2007) through combined use of EOF and wavelet analysis of satellite data, *Ocean Dyn.*, 61(1), 89–102.
- Organelli, E., A. Bricaud, D. Antoine, and J. Uitz (2013), Multivariate approach for the retrieval of phytoplankton size structure from measured light absorption spectra in the Mediterranean Sea (BOUSSOLE site), *Appl. Opt.*, 52(11), 2257–2273.
- Organelli, E., et al. (2016), A novel near-real-time quality-control procedure for radiometric profiles measured by bio-argo floats: Protocols and performances, *J. Atmos. Oceanic Technol.*, 33(5), 937–951, doi:10.1175/JTECH-D-15-0193.1.
- Pasqueron de Fommervault, O., F. D'Ortenzio, A. Mangin, R. Serra, C. Migon, H. Claustre, H. Lavigne, M. R. d'Alcalá, L. Prieur, and V. Taillandier (2015a), Seasonal variability of nutrient concentrations in the Mediterranean Sea: Contribution of Bio-Argo floats, *J. Geophys. Res. Oceans*, 120, 8528–8550, doi:10.1002/2015JC011103.
- Pasqueron de Fommervault, O., C. Migon, F. D'Ortenzio, M. Ribera d'Alcalá, and L. Coppola (2015b), Temporal variability of nutrient concentrations in the northwestern Mediterranean Sea (DYFAMED time-series station), *Deep Sea Res., Part 1*, 100, 1–12.
- Poulain, P.-M., R. Barbanti, J. Font, A. Cruzado, C. Millot, I. Gertman, A. Griffa, A. Molcard, V. Rupolo, and S. Le Bras (2007), MedArgo: A drifting profiler program in the Mediterranean Sea, *Ocean Sci.*, 3(3), 379–395.
- Pujo-Pay, M., P. Conan, L. Oriol, V. Cornet-Barthaux, C. Falco, J.-F. Ghiglione, C. Goyet, T. Moutin, and L. Prieur (2011), Integrated survey of elemental stoichiometry (C, N, P) from the western to eastern Mediterranean Sea, *Biogeosciences*, 8(4), 883–899.
- Ras, J., H. Claustre, and J. Uitz (2008), Spatial variability of phytoplankton pigment distributions in the Subtropical South Pacific Ocean: Comparison between in situ and predicted data, *Biogeosciences*, 5(2), 353–369.
- Rigual-Hernández, A. S., M. A. Bárcena, R. W. Jordan, F. J. Sierro, J. A. Flores, K. J. S. Meier, L. Beaufort, and S. Heussner (2013), Diatom fluxes in the NW Mediterranean: Evidence from a 12-year sediment trap record and surficial sediments, *J. Plankton Res.*, 35(5), 1109–1125.
- Romagnan, J.-B., L. Legendre, L. Guidi, J.-L. Jamet, D. Jamet, L. Mousseau, M.-L. Pedrotti, M. Picheral, G. Gorsky, and C. Sardet (2015), Comprehensive model of annual plankton succession based on the whole-plankton time series approach, *PLoS One*, 10(3), e0119219.
- Sakamoto, C. M., K. S. Johnson, and L. J. Coletti (2009), Improved algorithm for the computation of nitrate concentrations in seawater using an in situ ultraviolet spectrophotometer, *Limnol. Oceanogr. Methods*, 7(1), 132–143.
- Schmechtig, C., A. Poteau, H. Claustre, F. D'Ortenzio, J. Buck, and T. Carval (2015), Bio-Argo floats: Data management in progress. . . , *Rep., Ifremer, France*, doi:10.13155/35385. [Available at <http://archimer.ifremer.fr/doc/00254/36542/>.]
- Severin, T., P. Conan, X. Durrieu de Madron, L. Houpert, M. J. Oliver, L. Oriol, J. Caparros, J. F. Ghiglione, and M. Pujo-Pay (2014), Impact of open-ocean convection on nutrients, phytoplankton biomass and activity, *Deep Sea Res., Part 1*, 94, 62–71, doi:10.1016/j.dsr.2014.07.015.
- Severin, T., et al. (2017), Open-ocean convection process: A driver of the winter nutrient supply and the spring phytoplankton distribution in the Northwestern Mediterranean Sea, *J. Geophys. Res.*, 122, 4602–4633, doi:10.1002/2016JC012664.
- Shabrang, L., M. Menna, C. Pizzi, H. Lavigne, G. Civitarese, and M. Gačić (2015), Long-term variability of the South Adriatic circulation and phytoplankton biomass in relation to large-scale climatic pattern, *Ocean Sci. Discuss.*, 12, 203–226, doi:10.5194/osd-12-203-2015.
- Siegel, D. A., S. C. Doney, and J. A. Yoder (2002), The North Atlantic spring phytoplankton bloom and Sverdrup's critical depth hypothesis, *Science*, 296(5568), 730–733.
- Siokou-Frangou, I., U. Christaki, M. G. Mazzocchi, M. Montresor, M. Ribera d'Alcalá, D. Vaqué, and A. Zingone (2010), Plankton in the open Mediterranean Sea: A review, *Biogeosciences*, 7(5), 1543–1586, doi:10.5194/bg-7-1543-2010.
- Somot, S., et al. (2016), Characterizing, modelling and understanding the climate variability of the deep water formation in the North-Western Mediterranean Sea, *Clim. Dyn.*, 1–32, doi:10.1007/s00382-016-3295-0.
- Sverdrup, H. U. (1953), On conditions for the vernal blooming of phytoplankton, *J. du Cons.*, 18(3), 287–295.
- Taylor, J. R., and R. Ferrari (2011a), Ocean fronts trigger high latitude phytoplankton blooms, *Geophys. Res. Lett.*, 38, L23601, doi:10.1029/2011GL049312.
- Taylor, J. R., and R. Ferrari (2011b), Shutdown of turbulent convection as a new criterion for the onset of spring phytoplankton blooms, *Limnol. Oceanogr., Methods*, 56, 2293–2307.
- Testor, P., and J.-C. Gascard (2006), Post-convection spreading phase in the Northwestern Mediterranean Sea, *Deep Sea Res., Part 1*, 53(5), 869–893, doi:10.1016/j.dsr.2006.02.004.
- Testor, P., et al. (2010), Gliders as a component of future observing systems, in *Proceedings of OceanObs'09: Sustained Ocean Observations and Information for Society*, edited by J. Hall, D. E. Harrison, and D. Stammer, ESA Publ., WPP-306, pp. 961–978, doi:10.5270/OceanObs09.cwp.89.
- Testor, P., et al. (2017), Multi-scale observations of deep convection in the northwestern Mediterranean Sea during winter 2012–2013 using multiple platforms, *J. Geophys. Res. Oceans*, doi:10.1002/2016JC012671.
- The Mermex Group (2011), Marine ecosystems' responses to climatic and anthropogenic forcings in the Mediterranean, *Prog. Oceanogr.*, 91(2), 97–166, doi:10.1016/j.pocean.2011.02.003.
- Thomalla, S. J., M.-F. Racault, S. Swart, and P. M. S. Monteiro (2015), High-resolution view of the spring bloom initiation and net community production in the Subantarctic Southern Ocean using glider data, *ICES J. Mar. Sci.*, 72(6), 1999–2020.
- Thysen, M., G. J. Grégori, J.-M. Grisoni, M. L. Pedrotti, L. Mousseau, L. F. Artigas, S. Marro, N. García, O. Passafiume, and M. J. Denis (2014), Onset of the spring bloom in the northwestern Mediterranean Sea: Influence of environmental pulse events on the in situ hourly-scale dynamics of the phytoplankton community structure, *Front. Microbiol.*, 5, 387, doi:10.3389/fmicb.2014.00387.
- Townsend, D. W., L. M. Cammen, P. M. Holligan, D. E. Campbell, and N. R. Pettigrew (1994), Causes and consequences of variability in the timing of spring phytoplankton blooms, *Deep Sea Res., Part 1*, 41(5), 747–765.

- Uitz, J., D. Stramski, B. Gentili, F. D'Ortenzio, and H. Claustre (2012), Estimates of phytoplankton class specific and total primary production in the Mediterranean Sea from satellite ocean color observations, *Global Biogeochem. Cycles*, *26*, GB2024, doi:10.1029/2011GB004055.
- Volpe, G., B. B. Nardelli, P. Cipollini, R. Santoleri, and I. S. Robinson (2012), Seasonal to interannual phytoplankton response to physical processes in the Mediterranean Sea from satellite observations, *Remote Sens. Environ.*, *117*, 223–235.
- Waldman, R., S. Somot, M. Herrmann, A. Bosse, G. Caniaux, C. Estournel, L. Houpert, L. Prieur, F. Sevault, and P. Testor (2017), Modelling the intense 2012–2013 dense water formation event in the northwestern mediterranean sea: Evaluation with an ensemble simulation approach, *J. Geophys. Res. Oceans*, *122*, 1297–1324, doi:10.1002/2016JC012437.
- Xing, X., H. Claustre, S. Blain, F. D'Ortenzio, D. Antoine, J. Ras, and C. Guinet (2012), Quenching correction for in vivo chlorophyll fluorescence acquired by autonomous platforms: A case study with instrumented elephant seals in the Kerguelen region (Southern Ocean), *Limnol. Oceanogr. Methods*, *10*, 483–495.
- Zielinski, O., D. Voß, B. Saworski, B. Fiedler, and A. Körtzinger (2011), Computation of nitrate concentrations in turbid coastal waters using an in situ ultraviolet spectrophotometer, *J. Sea Res.*, *65*(4), 456–460.